2021-12-10

Quantitative STEM: A Method for Measuring Temperature and Thickness Effects on Thermal Diffuse Scattering Using STEM/EELS, and for Testing Electron Scattering Models

Paul S. Minson
Brigham Young University

Quantitative STEM: A Method for Measuring Temperature and Thickness Effects on Thermal Diffuse Scattering Using STEM/EELS, and for Testing Electron Scattering Models

Paul S. Minson

A thesis submitted to the faculty of
Brigham Young University
in partial fulfillment of the requirements for the degree of

Master of Science

Richard Vanfleet, Chair
Robert C. Davis
Jeffrey K. Farrer
Felipe Rivera

Department of Physics and Astronomy

Brigham Young University

ABSTRACT

Quantitative STEM: A Method for Measuring Temperature and Thickness Effects on Thermal Diffuse Scattering Using STEM/EELS, and for Testing Electron Scattering Models

Paul S. Minson
Department of Physics and Astronomy, BYU
Master of Science

In the last two decades, advances in the dark field detectors and microscopes of scanning transmission electron microscopy (STEM) have inspired a resurgence of interest in quantitative STEM analysis. One promising avenue is the use of STEM as a nanothermometric probe. In this application, thermal diffuse scattering, captured by a CCD camera or an annular dark field detector, acts as an indirect measurement of the specimen temperature. One challenge with taking such a measurement is achieving adequate sensitivity to quantify a change in scattered electron signal on the order of 1% or less of the full electron beam. Another difficulty is decoupling the thermal effect on electron scattering from scattering changes due to differing specimen thicknesses and materials. To address these issues, we have developed a method using STEM, combined with electron energy loss spectroscopy (EELS), to produce a material-specific calibration curve. On silicon, across the range 89 K to 294 K, we measured a monotonically increasing HAADF signal ranging from 4.0% to 4.4% of the direct beam intensity at a thickness-to-mean-free-path ratio of 0.5. This yielded a calibration curve of temperature versus full-beam-normalized, thickness-normalized HAADF signal. The method enables thermal measurements on a specimen of varying local thickness at a spatial resolution of a few nanometers. We demonstrated the potential of the technique for testing electron scattering models by applying single-electron scattering theory to the data collected to extract a measurement of the mean atomic vibration amplitude in silicon at 294 K. The measured value, 0.00738 ± 0.00002 nm, agrees well with reported measurement using X-rays.

Keywords: STEM, EELS, thermal diffuse scattering, TDS

ACKNOWLEDGMENTS

Thank you, Dr. Vanfleet, for your willingness to accept a non-traditional graduate student in unusual circumstances. Your patience, encouragement, and mentoring were invaluable, as was the sharing of your time, expertise, and library. I thoroughly enjoyed taking those classes from you about subjects so near and dear to my own heart.

Thank you, Dr. Davis. Your enthusiasm for research, creativity, and raw energy were an inspiration to me to keep going when things were difficult. The class I had from you stands as a monumental example that great teaching should not be restricted to the traditional format and can make the learning more interesting, engaging, and enjoyable.

Thank you, Dr. Farrer. Your support and encouragement for my pursuit of this degree was what made it possible. Your own example of changing disciplines between your undergraduate and graduate work showed me the possibilities and gave me hope for my own effort. And all the advice and insight you provided have contributed immeasurably to both my graduate and professional career at BYU.

Thank you, Dr. Rivera. Despite being a recent addition to my committee, you were a life-saver! Your just-in-the-nick-of-time critique, feedback, and advice has made this thesis and the accompanying paper much better works. And probably saved some of what little hair I have left!

Finally, thank you to my family for being willing to sacrifice so much to enable me to reach this milestone. Thank you, Johanna-Maria, for supporting me in numerous ways and encouraging and loving me through it all. Thank you, Thomas, Kristiina, Michelle, and Matthew for your patience and understanding during this long process. I literally could not have done it without you all.

TABLE OF CONTENTS

LIST OF FIGURES

1 Introduction

Dark field STEM (DF-STEM) has typically been used as a non-quantitative imaging technique. Because the scattered electrons used to construct STEM images carry information about the specimen at the location where they passed through it, DF-STEM offers the possibility of doing quantitative analysis of specimens with very high spatial resolution using the absolute or relative scattered electron signal as a direct or indirect measure of a specimen property. In the recent two decades, the advent of high efficiency DF-STEM detectors and probe corrected microscopes has inspired David Muller at Cornell, Susan Stemmer at UC Santa Barbara, and others to explore this potential. [1–7] This has proved challenging, in part due to the convolution of a variety of factors—such as specimen temperature, thickness, and composition—that influence the scattered electron intensity in DF-STEM. Extraction of information from the signal often requires deconvolution of these effects to yield quantitative analysis results.

One application for such analysis is in the field of nanothermometry. As electronic and MEMs devices continue to shrink, with feature sizes well below 100 nm in some applications, thermal design and management in such devices drives a growing need for nanoscale temperature measurements. Previously used common, non-STEM techniques like microthermocouples, liquid crystal thermography, and others reviewed by Christofferson et al. all suffer various limitations in spatial resolution, response time, flexibility, practicality, etc. [8] Over the last decade, interest has increased in measuring electron scattering in a transmission electron microscope (TEM) in scanning mode (STEM) to perform in situ nano-

thermometry on a specimen as a potential solution to the needs. It is desirable that a TEM-based nanothermometry method provide high spatial resolution and, for maximum flexibility in application, an accommodation of specimen thickness variation. Egoavil et al. confirmed experimentally that electron-phonon interactions are highly localized, which potentially permits sub-nanometer spatial resolution of information from those interactions. [9] Idrobo et al. investigated using STEM in conjunction with an expensive, monochromated microscope and EELS system to assess local specimen temperature using phonon energy gain and loss peaks, which while successful, lacked high spatial resolution owing to the aloof configuration, and required high energy resolution EELS using a monochromated beam. [10] He & Hull conducted investigation into the use of thermal diffuse scattering (TDS) in the TEM as a potential signal for nanoscale temperature measurements. [11] Using a very large beam and rather thick specimens, they found that specimen thickness played a significant role in the thermometry signal, complicating TDS measurement and requiring "that potential nanoscale temperature measurements using TDS of electrons in the TEM need to be 'tuned' (in sample thickness and collection angle) for greatest sensitivity for a particular material." Additionally, their method required a specimen of known, uniform thickness. Wehmeyer et al. used STEM to measure specimen temperature by assessing TDS on convergent beam electron diffraction (CBED) patterns with elastic scattered electrons excluded through virtual apertures, but their method also necessitated uniform specimen thickness. [12]

Here we present a method for obtaining thermal measurements using a standard STEM-capable, HAADF- and EELS-equipped microscope that addresses the issues with spatial resolution and specimen thickness. The method permits nanometer-resolution spatial temperature measurements, while normalizing to local specimen thickness through

a self-aligned thickness measurement at each sampling location. Our method shows potential for testing of electron scattering models as well, as demonstrated by extraction of a measurement of the mean atomic vibration amplitude of silicon using a single-electron scattering model. Data in the method is collected by acquisition of a map on the specimen, simultaneously collecting HAADF signal and an EELS spectrum at each point. This is followed by post-processing to get scattered electron signal normalized to the full beam, and specimen thickness normalized to the electron mean free path in the specimen. A limitation of the method is that a material-specific temperature calibration must be made for each specimen material to be measured.

2 Theory

2.1 Thermal Diffuse Scattering (TDS)

The temperature dependence of TDS, combined with the availability of multiple types of electron detectors in a STEM, makes STEM measurement of TDS a potential candidate for nanothermometry. Thermal diffuse scattering occurs when electrons scatter from an electron beam passing through the specimen due to thermal vibration of atoms around their equilibrium positions in the specimen. The mean atomic vibration amplitude $\langle u_s \rangle$ characterizes this displacement. Although technically an inelastic process, the scattering can be regarded as quasi-elastic scattering of the electron from a stationary distorted lattice because the interaction time with a specimen by a beam electron having typical TEM energies is approximately two orders of magnitude shorter than the atomic thermal vibration period. [13] These scattered electrons appear in the diffuse background of the specimen's diffraction pattern in reciprocal space, as shown in Figure 2-1. This diffuse

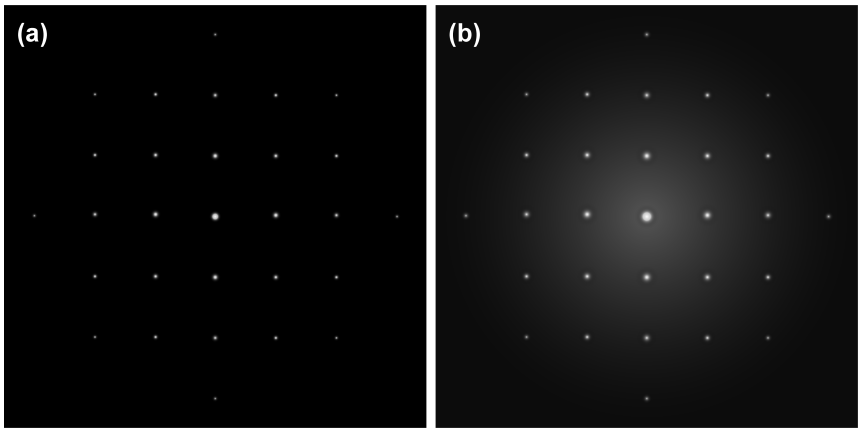

Figure 2-1: Schematic representation of the effect of thermal diffuse scattering on a diffraction pattern. (a) A hypothetical [001] diffraction pattern from an idealized FCC crystal with all atoms precisely on their lattice positions. (b) The same pattern, but with the effects of thermal diffuse scattering illustrated. The direct beam and each diffracted beam have an approximately Gaussian skirt of diffuse intensity. The direct beam's much higher intensity means its skirt is correspondingly more intense, dominating the background between diffraction spots.

scattering is present even at 0 K due to low-but-non-zero atomic motion arising from the zero-point energy. As the specimen temperature rises, $\langle u_s \rangle$ rises and typically the amount of scattering increases significantly. This scattering has been found to be insensitive to tilt, and can be measured to assess specimen temperature. [11]

2.2 Measuring Electron Scattering Using the HAADF

Prevalent in STEM, the high-angle annular dark field detector (hereafter referred to as the 'HAADF') offers the potential for quantitative or semi-quantitative measurement of scattered electrons, without modification to the detector or incorporation of additional specialized hardware on a microscope so-equipped.

The signal measured by the HAADF is a core part of the technique presented. We will refer to signals from the HAADF using a boldface capital '**S**'. The purpose of the boldface is to alleviate confusion with the scattering vector which also appears in this document. From wave scattering theory, the scattering vector is traditionally noted as a lowercase 's' and defined as $s = \sin(\theta)/\lambda_B$, where θ is the scattering half-angle and λ_B is the wavelength of the scattered wave. [14] (Note: technically s is the magnitude of the scattering vector; in the literature the nomenclature is used to refer to both the actual vector and its magnitude, and we here follow the literature convention.)

An idealized case is instructive in illustrating the thermal influence on the scattered electron signal change measured when specimen temperature is altered. For simplicity, we assume a two-beam condition such as that used in the Debye model, and a camera length selected so that a negligible amount of TDS passes through the HAADF inner aperture, with a sufficiently large detector annulus outer diameter such that a negligible quantity of scattered electrons passes beyond the outer HAADF angle. For a given beam location on the

specimen, at two different specimen temperatures $T1$ and $T2$, we assign $\boldsymbol{S}_{T1}$ and $\boldsymbol{S}_{T2}$ as the signal measured on the HAADF from that specimen location. Then the difference in signal $\Delta\boldsymbol{S}$ seen on the HAADF at the two temperatures is:

$$\Delta\boldsymbol{S} = \boldsymbol{S}_{T2} - \boldsymbol{S}_{T1} \tag{2-1}$$

The electron signal ($\boldsymbol{S}$) impinging on the detector at those temperatures is composed of the elastically scattered (diffracted beam) signals E_{T1} and E_{T2}, the scattered TDS signals I_{T1} and I_{T2}, and other specimen-temperature-independent scattering mechanisms represented by Y. Therefore

$$\boldsymbol{S}_{T1} = I_{T1} + E_{T1} + Y \tag{2-2}$$

$$\boldsymbol{S}_{T2} = I_{T2} + E_{T2} + Y \tag{2-3}$$

and Equation (2-1) becomes

$$\Delta\boldsymbol{S} = I_{T2} + E_{T2} + Y - (E_{T1} + I_{T1} + Y) \tag{2-4}$$

At each of the two temperatures, the scattered signal (I) impinging on the detector has two components: scattering from the primary beam $I_{B,T1}$, $I_{B,T2}$ (the subscript 'B' here denotes the primary beam) and scattering from the diffracted or elastically scattered beam $I_{E,T1}$ and $I_{E,T2}$ (the subscript E denotes the diffracted beam), so that

$$I_{T1} = I_{B,T1} + I_{E,T1} \tag{2-5}$$

$$I_{T2} = I_{B,T2} + I_{E,T2}$$

(2-6)

From the Debye model, we have that the temperature-adjusted, elastically-scattered signals E_{T1} and E_{T2} are equal to the diffracted signal E_{B0} from a perfect, non-thermally-distorted crystal multiplied by a Debye-Waller factor for each specimen temperature W_{T1} and W_{T2}, giving diffracted beam signals of

$$E_{T1} = W_{T1}E_{B0}$$

(2-7)

$$E_{T2} = W_{T2}E_{B0}$$

(2-8)

Substituting Equations (2-5), (2-6), (2-7), and (2-8) into Equation (2-4) gives

$$\Delta \boldsymbol{S} = I_{B,T2} + I_{E,T2} + W_{T2}E_{B0} + Y - (I_{B,T1} + I_{E,T1} + W_{T1}E_{B0} + Y)$$

(2-9)

Finally, we note that the scattering from the diffracted beam is the balance of the diffracted beam signal from the perfect, non-thermally-distorted crystal, so

$$I_{E,T1} = (1 - W_{T1})E_{B0}$$

(2-10)

$$I_{E,T2} = (1 - W_{T2})E_{B0}$$

(2-11)

Plugging these expressions into Equation (2-9) produces

$$\Delta \boldsymbol{S} = I_{B,T2} + (1 - W_{T2})E_{B0} + W_{T2}E_{B0} + Y - (I_{B,T1} + (1 - W_{T1})E_{B0} + W_{T1}E_{B0} + Y)$$

(2-12)

Distributing gets an intermediate expression

$$\Delta \boldsymbol{S} = I_{B,T2} + E_{B0} - W_{T2}E_{B0} + W_{T2}E_{B0} + Y - I_{B,T1} - E_{B0} + W_{T1}E_{B0} - W_{T1}E_{B0} - Y$$

(2-13)

and combining like terms yields the result

$$\Delta S = I_{B,T2} - I_{B,T1}$$

(2-14)

showing that, to first order, the change in HAADF signal measured at the two temperatures is primarily due to the change in thermal diffuse scattering out of the primary beam.

2.3 Measuring Specimen Thickness Using EELS

To measure specimen temperature using TDS requires distinguishing the impact of specimen thickness on TDS signal from the effect of temperature on the TDS signal. To separate the two, a measure of the specimen thickness parallel to the primary beam was needed. Measurement of specimen thickness using EELS became another core part of the technique presented. The specimen thickness, normalized to the mean free path of electrons in the specimen, was measured using the method described by Egerton. [15] In this method the thickness normalized to the effective mean free path in the material is obtained from an EELS spectrum using the relationship

$$(t/\lambda) = \ln(I_t/I_0)$$

(2-15)

where t is the absolute specimen thickness, λ is the effective mean free path of the electron in the specimen between inelastic scattering events accounting for the EELS collection angle, I_t is the total intensity of the spectrum, and I_0 is the intensity of the zero-loss peak (ZLP). In practice, on collected spectra it is necessary to define the energy width for integration of the

ZLP, and to ensure that the upper energy bound for integration of the whole spectrum is sufficiently high such that any omitted intensity beyond that point is negligible.

2.4 Extracting Temperature from Electron Scattering

Because TDS is an indirect measure of the specimen temperature, calibration is required to obtain a temperature measurement from TDS signals. This allows us to get quantitative results from a technique (STEM) that historically has been primarily used for qualitative imaging. To simplify notation, we define the normalized HAADF signal as $\boldsymbol{S}_{norm} = \boldsymbol{S}/\boldsymbol{S}_0$ where $\boldsymbol{S}_0$ is the HAADF signal when the full beam impinges on the detector and $\boldsymbol{S}$ is HAADF signal level for a point on the specimen at a given temperature T. We then expect, according to semi-classical two-beam theory and using the thin specimen approximation, that the amount of TDS will be proportional to the sample thickness for a thin specimen. [16] This leads to the expectation that $\boldsymbol{S}_{norm}$ should be related to the product of specimen thickness and some function of temperature $f(T)$. Incorporating the measured normalized thickness (t/λ) defined in Equation (2-15), the expected relationship becomes $\boldsymbol{S}_{norm} = D \cdot f(T) \cdot (t/\lambda)$, where D is an empirical calibration constant. Rearrangement gives

$$D \cdot f(T) = \boldsymbol{S}_{norm}/(t/\lambda) \tag{2-16}$$

suggesting that the calibration constant D and the dependence on temperature can be obtained by fitting a curve to measurements of $\boldsymbol{S}_{norm} / (t/\lambda)$ at multiple specimen temperatures and thicknesses. Doing so normalizes out the thickness effect while retaining the temperature dependence. Once determined, this relationship can be solved for T, yielding a calibrated expression for measurement at points of interest of local specimen temperature through $\boldsymbol{S}_{norm}$ and (t/λ) measurements.

3 Experiment

3.1 The Microscope and Its Settings

Data was collected on a Thermo Fisher Scientific Tecnai F20 G2 S-TEM equipped with an UltraTwin lens, Fischione Model 3000 HAADF, and Gatan Tridiem GIF/EELS system. [17,18] The specimen holder was a Gatan Model 636.DH liquid-nitrogen-cooled holder. Collection of two-dimensional maps of simultaneous HAADF signal and EELS spectra was found to be the most expedient method of gathering the required data. Use of this method allowed internal calibration information to be collected with each map, but it did complicate the setup work on the microscope, as described below.

In electron microscopy, the rule is that almost everything is a trade-off. This experiment was no exception. A number of competing constraints needed to be satisfied to make the technique work, which required careful selection of the microscope parameters, as follows.

3.1.1 Electron Gun, Condenser, and Apertures

Critical interrelated and somewhat opposing concerns to address were detector signal-to-noise and saturation for both HAADF and EELS. High probe current was desirable to acquire sufficient HAADF signal in a reasonable collection time, but to prevent saturation of the EELS CCD camera, direct beam current into the EELS entrance aperture had to be limited. Saturation on the EELS caused a loss of ZLP signal which manifested as a flattened top on the ZLP of the EELS spectrum, rendering the thickness measurement inaccurate under saturation conditions. EELS entrance aperture diameter was selected based on the need to

avoid EELS saturation at a beam current providing sufficient HAADF signal, while still getting adequate EELS signal-to-noise and maintaining good energy resolution on the ZLP (<1 eV FWHM). Gun Lens 5 and Spot 9 in STEM mode, with a 100 μm Condenser 2 aperture, was found to give good signal on the HAADF. These combined nicely with a 1 mm entrance aperture on the EELS to keep the beam current striking the energy filter CCD camera below its saturation intensity. Under these conditions, an energy resolution of 0.73 eV was seen on the ZLP—quite adequate for the intended measurements.

3.1.2 STEM Camera Length

Selection of camera length was important, and as illustrated in Figure 3-1, involved a compromise. Several factors favored a short camera length. First, it would maximize the angle subtended by the HAADF to enhance high-angle TDS electron collection. Second, it would serve to minimize the low-angle diffracted electron signal striking the HAADF. Further, some small displacement of the CBED pattern was seen during scanning, which we attributed to incomplete decoupling of beam shift and tilt. This produced a slight rocking of the beam as it scanned, and a corresponding shifting of the CBED pattern features. This movement increased with increasing scan dimensions. A short camera length would minimize the intensity of the CBED diffraction pattern features straddling the inner HAADF detector edge, thereby limiting the impact of their movement on the HAADF signal. A final benefit is to minimize the shift of the direct beam spot relative to the EELS entrance aperture.

However, a long camera length was desirable to limit the loss of the highest-intensity, low-angle thermally scattered electrons through the HAADF annulus central aperture, and to restrict the intensity entering the EELS aperture to prevent saturation.

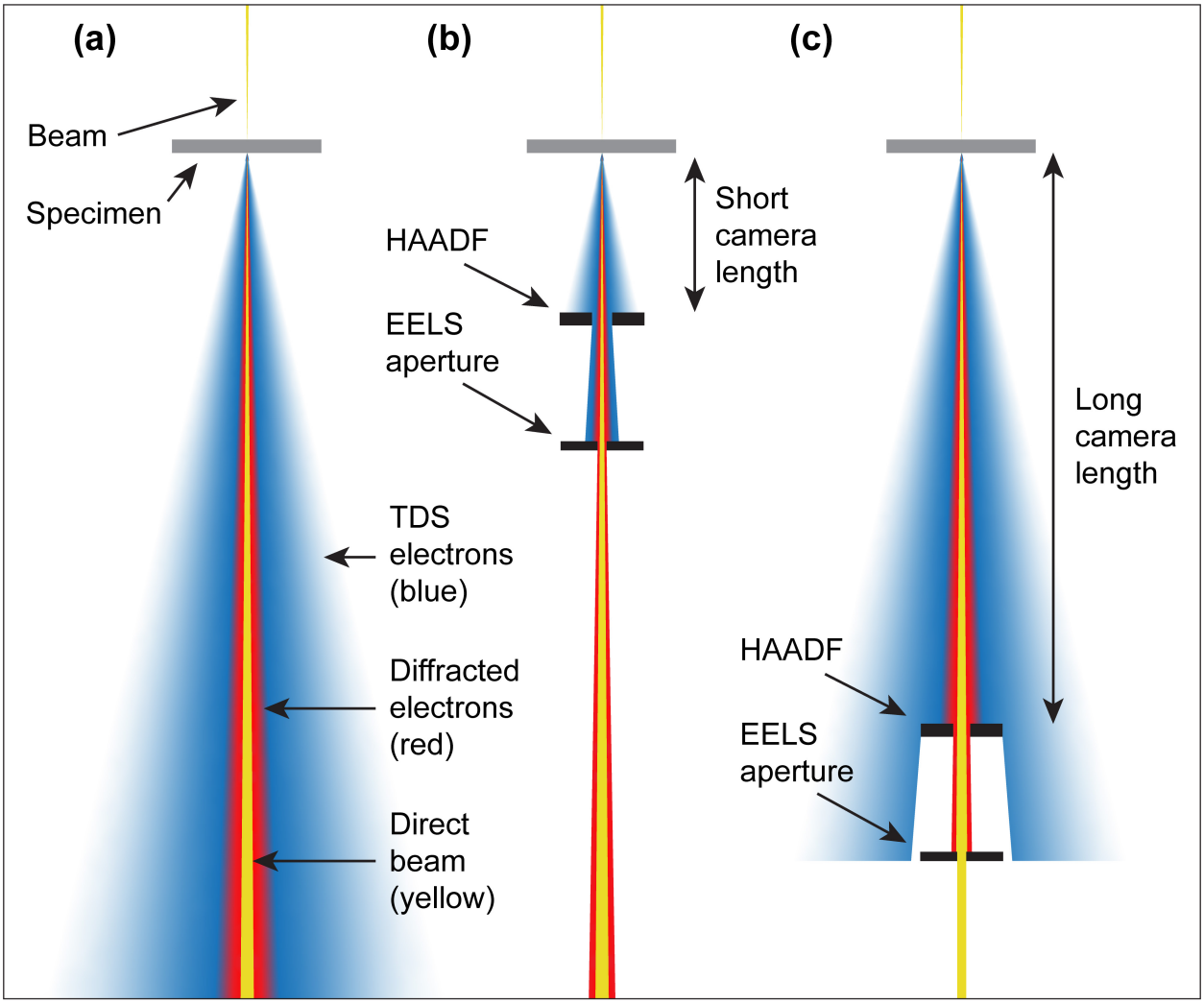

Figure 3-1: Schematic showing the trade-offs in camera length (CL) selection. a) STEM beam passing through a specimen, with the unscattered direct beam (yellow), diffracted electrons (red), and TDS electrons (blue) emerging. b) An inappropriately short CL gives the HAADF a wide collection angle for TDS electrons. It minimizes diffraction signal, but loses some of the highest intensity TDS signal through its center aperture, and admits excessive intensity into the EELS aperture. c) An inordinately long CL collects a lot of diffraction signal—degrading the signal-to-noise ratio—and loses large-angle-scattered TDS electrons. The optimal CL lies between the extremes shown.

Ensuring good sensitivity to TDS for the temperatures used in the experiment was critical. As calculated by Wang, around room temperature the elastically scattered electrons dominate the scattering signal for a scattering vector s less than 10 nm^{-1}, and TDS dominates the signal for s greater than 12.5 nm^{-1}. [14] This indicated that a camera length providing a range of collection angles where $s \geq 12.5$ nm^{-1} would be ideal. For our instrument, testing

found an indicated camera length of 220 mm on the instrument (actual camera length at the bottom mount CCD camera measured 301 mm) to be a good compromise for all the factors involved. At that camera length, the HAADF captured electrons scattered between 30.0 mrad and 199 mrad (1.7° and 11.4°) from the primary beam, corresponding to a scattering vector range of 5.98 $nm^{-1} < s < 39.6\ nm^{-1}$.

The chosen camera length also provided a large margin against the potential scan decoupling issue for both the HAADF and EELS system, as illustrated in Figure 3-2. The inner diameter of the HAADF annulus measured 60.1 mrad, with the direct beam spot having a diameter of 24.9 mrad, allowing the spot to displace more than a full radius during scanning without impinging on the HAADF. The EELS entrance aperture at this camera length

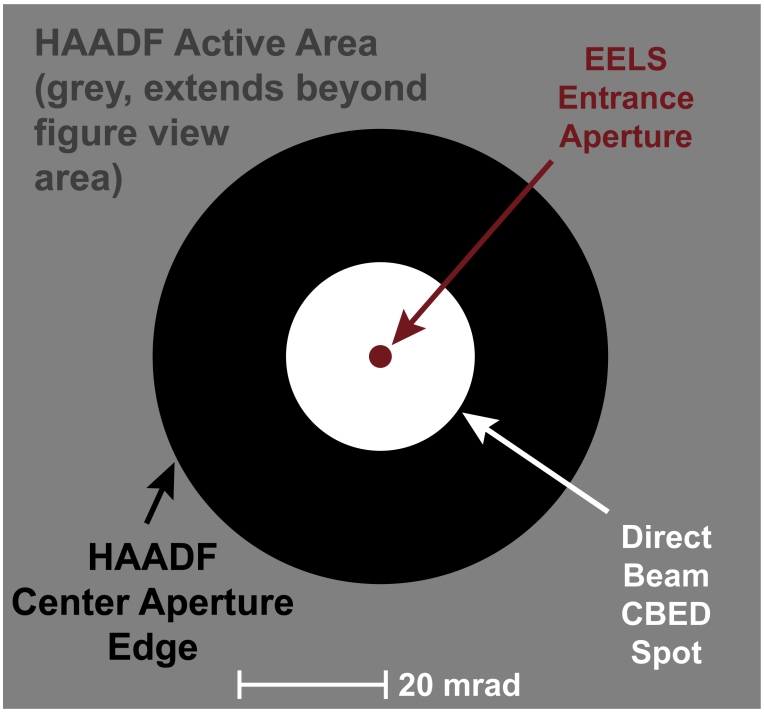

Figure 3-2: Scale comparison of direct beam spot size to HAADF aperture and EELS aperture diameters at a camera length of 220mm on our instrument. HAADF outer diameter extends beyond the page, it measured 398 mrad.

subtended 3.0 mrad, permitting the direct beam spot to displace by 87% of its radius and still fully cover the EELS aperture.

3.1.3 HAADF Setup

Quantitative measure of the scattered electron signal—relative to the full beam—required special setup of the HAADF detector parameters. The 16-bit HAADF has a limited dynamic range, and its output signal is modulated by the detector 'brightness' and 'contrast' settings in the microscope control software. To avoid saturation at either extremity of signal it was necessary to adjust the HAADF brightness and contrast levels for the selected experimental beam conditions.

A simple process was used to identify those settings so that the detector dark signal (i.e., with no scattered electrons striking it) and the detector bright signal (i.e., with 100% of the beam electrons striking it) would be contained within its dynamic range while spanning most of that range. The procedure was performed without a specimen under the beam. First, the system was set to dark conditions by putting the beam entirely through the HAADF inner diameter (so no electrons were impinging on the HAADF). Then the brightness and contrast were adjusted to place the detector signal slightly above the minimum detector output level including the noise, so at no point was the signal truncated. Next, the microscope was set to bright conditions by shifting the full beam onto the HAADF annulus and the signal adjusted to just below the maximum output level, again using the brightness and contrast controls and avoiding signal truncation. This procedure was iterated until satisfactory settings for the brightness and contrast were reached.

3.2 The Specimen, Temperatures, and Tilt

The specimen used was a tripod-polished wedge from a (100) silicon wafer, with the thin axis of the wedge oriented parallel to the [001] direction. Mounted on a copper washer, the specimen was placed in the Gatan cold holder such that the [001] axis was parallel to the beam, the [100] direction was aligned parallel to the stage X-axis, and the [010] direction aligned parallel to the Y-axis.

Multiple maps were taken of the same selected area on the specimen at each of four temperatures: 294 K, 88 K, 157 K, 225 K, and again at 294 K, in that order. The selected experimental temperatures were uniformly distributed across the operating range of the holder. Whenever the specimen holder temperature was changed, a minimum of 30 minutes was allowed before collecting the next map. This ensured that the specimen had time to equilibrate at the new temperature. At each temperature, two off-zone maps were acquired. To position the specimen off-zone, it was tilted approximately 5.0 degrees off the [001] zone axis to an orientation of low overall diffracted intensity as determined by inspection of the diffraction pattern and kikuchi bands. This was achieved by starting on-zone, and then tilting +4.4° around the [100] axis (the X-axis) and +2.4° around the [010] axis (the Y-axis) using the stage α-tilt and β-tilt controls, respectively. This off-zone orientation improved the TDS sensitivity by increasing the proportion of thermally scattered electrons relative to elastically scattered electrons in the total HAADF signal. Because of thermal expansion/contraction effects on the holder and specimen, the specimen orientation had to be adjusted and verified prior to each map acquisition, reproducing the previously-obtained kikuchi band pattern and diffraction pattern. Two on-zone [001] maps were also acquired at each temperature, but these yielded poor results for reasons described in Chapter 4.

3.3 Map Collection

After setting up the HAADF, the specimen was stabilized at the desired temperature, the area of interest was located, and any adjustments to tilt were done. A map was then defined and collected. The map dimensions selected for use were 24 pixels wide by 7 pixels high. Dwell time for each pixel in a map was 500 milliseconds. After a change to a new, stabilized specimen temperature, the locate-and-tilt process had to be repeated for the area of interest due to thermal effects as explained above.

Although ease and speed made it tempting to collect a single pair of HAADF dark signal and bright signal reference values for the experiment at the outset—prior to any map acquisitions—we felt it wise to do map-specific dark and bright calibration of the HAADF response to account for any drift in the beam current or change in the HAADF sensitivity over time. This was done on each map during data collection by allowing the beam to scan off the edge of the specimen on each row, yielding several map pixels in each row having zero scattered electron signal (i.e., a dark reference for that map). Then, for the fifth row of the map, the specimen was shifted completely out from under the beam and the direct beam spot was shifted onto the HAADF to yield the full beam signal (i.e., the bright reference for that map). This condition was maintained for the final two rows. (See Figure 3-3 for an example map produced by this process.) The dark and bright reference pixels were then utilized in the post-processing of the map.

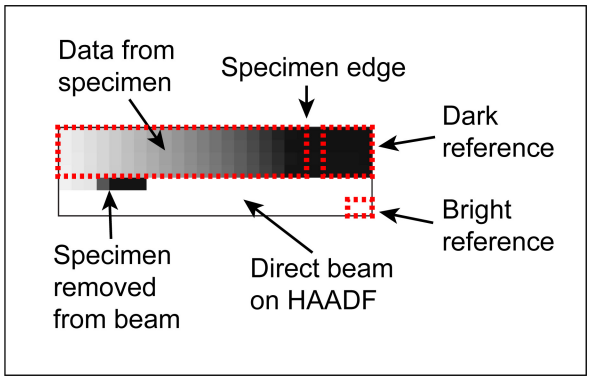

Figure 3-3: Example of a map, showing the upper 4 rows containing specimen signal and the dark reference (each outlined in red); the 5th sacrificial row (used to remove specimen from under beam and shift full beam onto the HAADF); and the lowest 2 rows, with the full beam on the HAADF, containing the bright reference (also outlined in red). Rows are scanned left-to-right, starting with the top row and going downward.

3.3.1 Post-Acquisition Map Processing

The collected maps combining HAADF signal and EELS spectra were processed using the Tecnai Imaging and Analysis software application (TIA) and a MATLAB script to extract a dataset consisting of a normalized HAADF signal versus normalized thickness.

From each map a reference zero-beam signal $\boldsymbol{S_{dark}}$ for that map was extracted manually using TIA, by averaging the dark reference pixels where the beam was not on the specimen and thus not being scattered onto the HAADF. A full beam reference signal $\boldsymbol{S_{full}}$ was taken for each map from the final pixel recorded after the full beam was shifted onto the HAADF scintillator. These values along with the map data were then supplied to the script for processing. (See Appendix A for details of the script use and code.)

The script combined the HAADF signal for each pixel in the map $\boldsymbol{S_{pixel}}$ with that map's zero- and full-beam signals to give a normalized signal S/S_0 for that pixel:

$$\boldsymbol{S/S_0 = (S_{pixel} - S_{dark})/(S_{full} - S_{dark})} \tag{3-1}$$

The script calibrated the zero-loss peak for the EELS spectrum from each map pixel by applying a Gaussian fit to identify the ZLP center, and then shifting the zero of the energy scale to place the peak at 0 eV. It subsequently calculated the normalized specimen thickness (t/λ) for that pixel location on the sample.

To calculate the normalized thickness, after calibrating the EELS spectrum to place the ZLP peak at 0 eV we followed [19] in integrating the ZLP from -3 eV to 3 eV to give the ZLP intensity I_0. The inelastic scattered intensity I_{in} was computed by integrating the inelastic scattered signal above 3 eV. The upper limit of the spectrum energy used for integration was 92.5 eV. See Figure 3-4 for an example EELS spectrum from this research. We then calculated the normalized specimen thickness from the relationship (which is simply a restatement of Equation (2-15) in different form):

$$(t/\lambda) = \ln(1 + I_{in}/I_0) \tag{3-2}$$

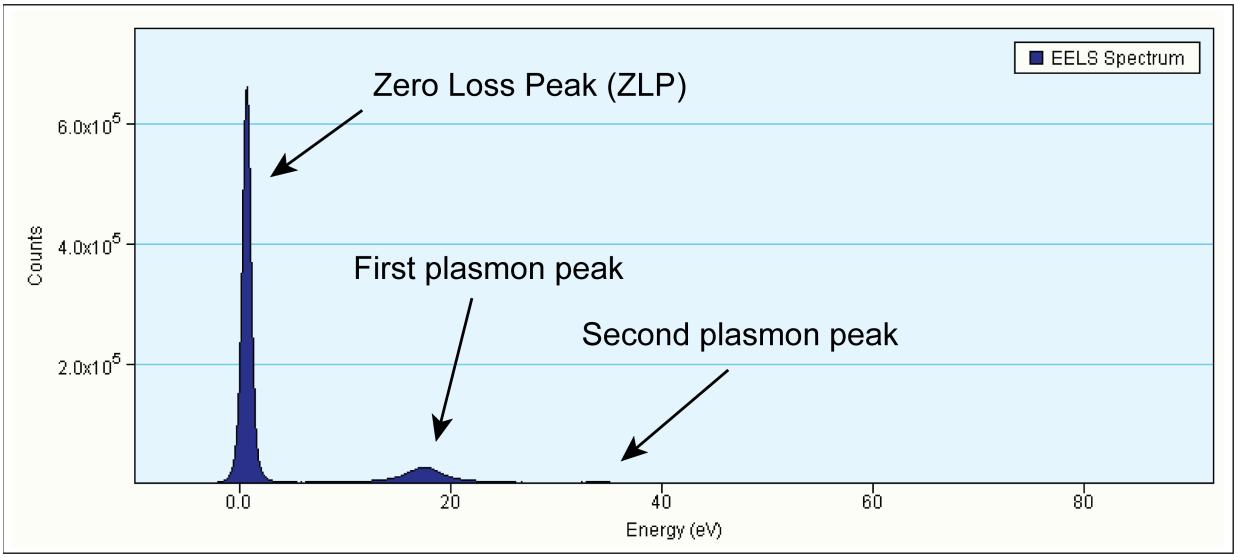

Figure 3-4: Example EELS spectrum from run A of the experiment, row 1, point 15, showing the zero loss peak and other features. Note that the ZLP is not correctly centered at 0 eV. The script used to process the data automatically corrected this condition.

It is worth noting that Equation (3-2) is a restatement of Lambert's Law of attenuation, in terms of the electron mean free path λ rather than an attenuation coefficient. In this case, the attenuation mechanism is scattering of the electron beam.

4 Results and Discussion

4.1 Maps

A total of 21 separate STEM/EELS maps were acquired for this experiment, excluding those captured during development of the technique. A summary of the various map runs and their conditions is given in Figure 4-1. Temperatures are rounded to the nearest integer.

Run ID	Temperature (K)	Tilt (On or Off Zone)		Run ID	Temperature (K)	Tilt (On or Off Zone)
A	294	off		L	157	off
B	294	off		M	157	off
C	295	near		N	157	on
D	295	near		O	157	on
E	295	on		P	225	off
F	295	on		Q	225	off
G	89	off		R	225	on
H	89	off		S	225	on
I	88	on		T	293	off
J	88	on		U	293	off
K	88	off				

Figure 4-1: The experimental runs and their conditions.

A STEM image of the specimen area where the maps were collected is given in Figure 4-2, along with a representative map acquired at room temperature. A distinctive polishing scratch in the specimen (visible in the upper portion of the image in Figure 4-2a) was used as a locator to ensure that all the data was collected from the same region of the sample. Images of this area were monitored for any evidence of carbon deposition during the experiment, to guard against alteration of the specimen thickness (or material!) at the sampled location. No detectable carbon deposition was seen.

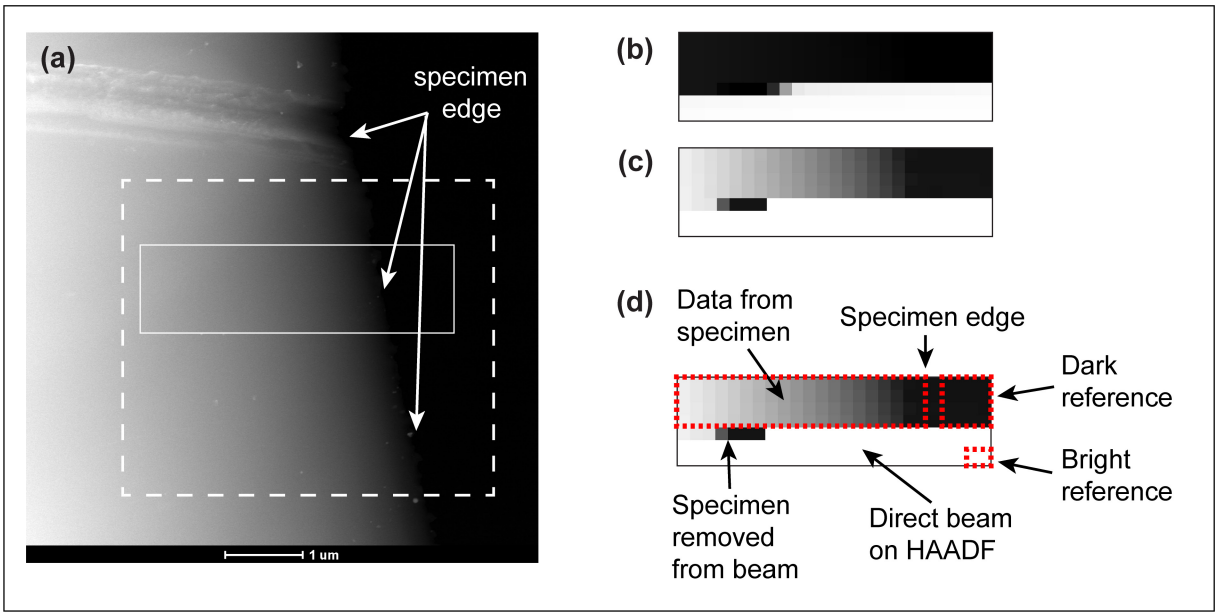

Figure 4-2. Specimen and data collection examples. (a) STEM image of [001] silicon wedge specimen edge, with the general data collection area outline by a hashed rectangle, and the location where the map in b and c was acquired marked with the solid rectangle. (b) The acquired HAADF signal map. (c) Same map as b but gamma-adjusted to make visible the gradient in the HAADF signal corresponding to specimen thickness gradient (thicker on the left). (d) Reminder of the anatomy of a map from Figure 3-3, showing the upper 4 rows containing specimen signal and dark reference; the 5th sacrificial row; and the lowest 2 rows containing the bright reference.

4.2 Off-Zone Scattered Electron Signal vs. Thickness

The results of the measurements for each temperature at the off-zone orientation of the specimen are plotted in Figure 4-3 (294 K), Figure 4-4 (225 K), Figure 4-5 (157 K), and Figure 4-6 (89 K). The normalized HAADF signal was below 10% of the full beam signal for all measured specimen thicknesses, which ranged from a (t/λ) of zero to a (t/λ) of approximately 1.0. As predicted by electron scattering theory and the thin specimen approximation (which is valid up to a (t/λ) of approximately 1.0), plots of normalized HAADF signal versus normalized thickness exhibited a linear behavior up to approximately a normalized thickness of 1.0 for each temperature. [16]

The runs from 157 K and 89 K (Figure 4-5 and Figure 4-6) show a slight divergence in the data between runs above approximately (t/λ) of 0.5. The cause is not known, but it

may be due to a small shift in the CBED pattern on the HAADF or dynamical scattering effects. Because of this, in analysis of the data to determine the temperature effect on TDS, we limited the data used for those calculations to points where (t/λ) was less than 0.5, staying in the regime where the thin specimen approximation is valid and minimizing dynamical scattering effects on the measurement.

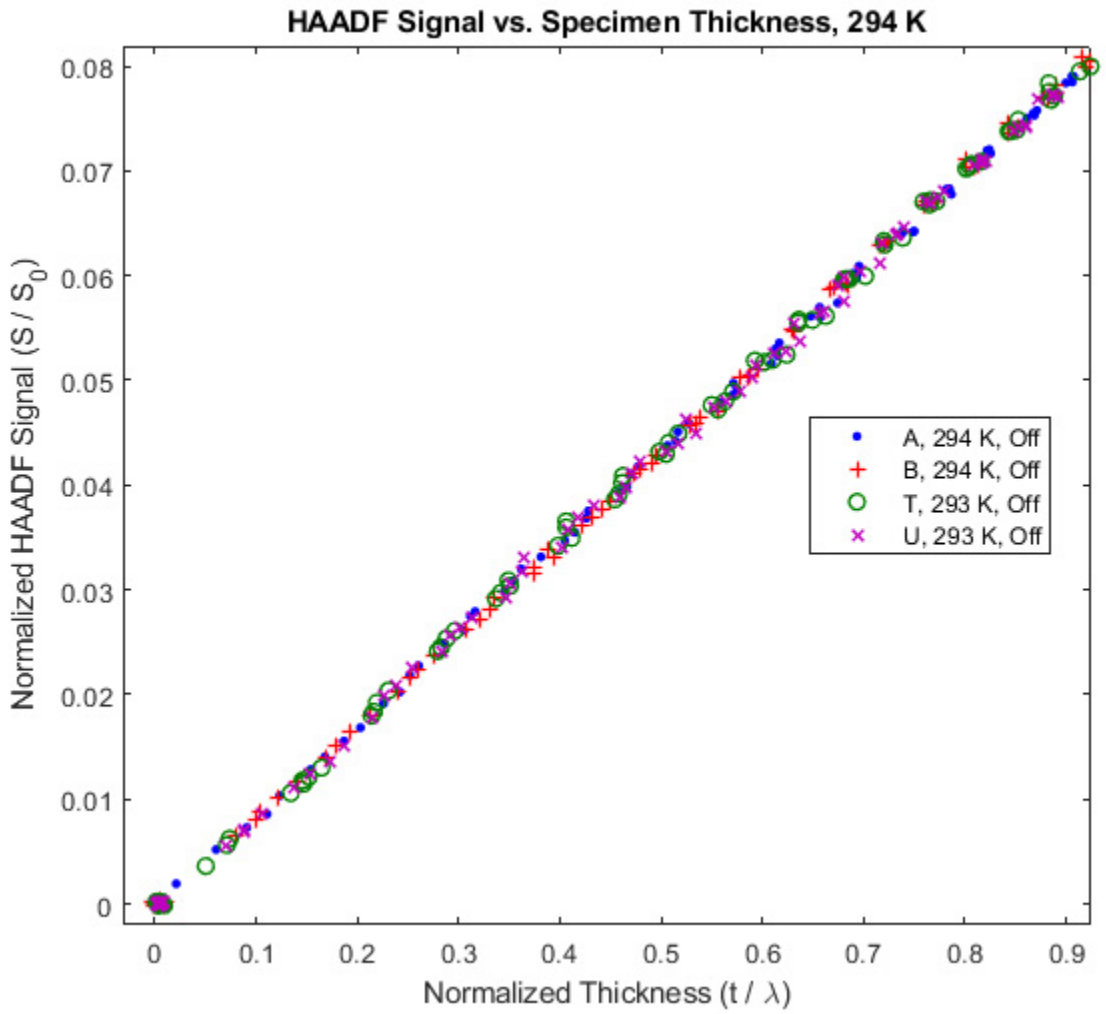

Figure 4-3. Plot of the HAADF signal (normalized to the full beam signal) versus specimen thickness (normalized to the mean free path of the beam electrons, as measured using EELS spectra) for four different maps collected on silicon at room temperature (294 K). Nicely linear across the measured range of thicknesses, the data matches the results expected from theory in the thin-specimen approximation. [15] The letter in the legend is the experimental run identifier; 'Off' indicates the data was acquired with the specimen tilted 5° off the [001] zone.

In the room temperature results of Figure 4-3, as a check for stability and repeatability, runs A and B were taken as the first data of the experiment, and runs T and U were collected six and a half hours later at the end of the experiment. They appear indistinguishable when overlaid, confirming good stability and repeatability.

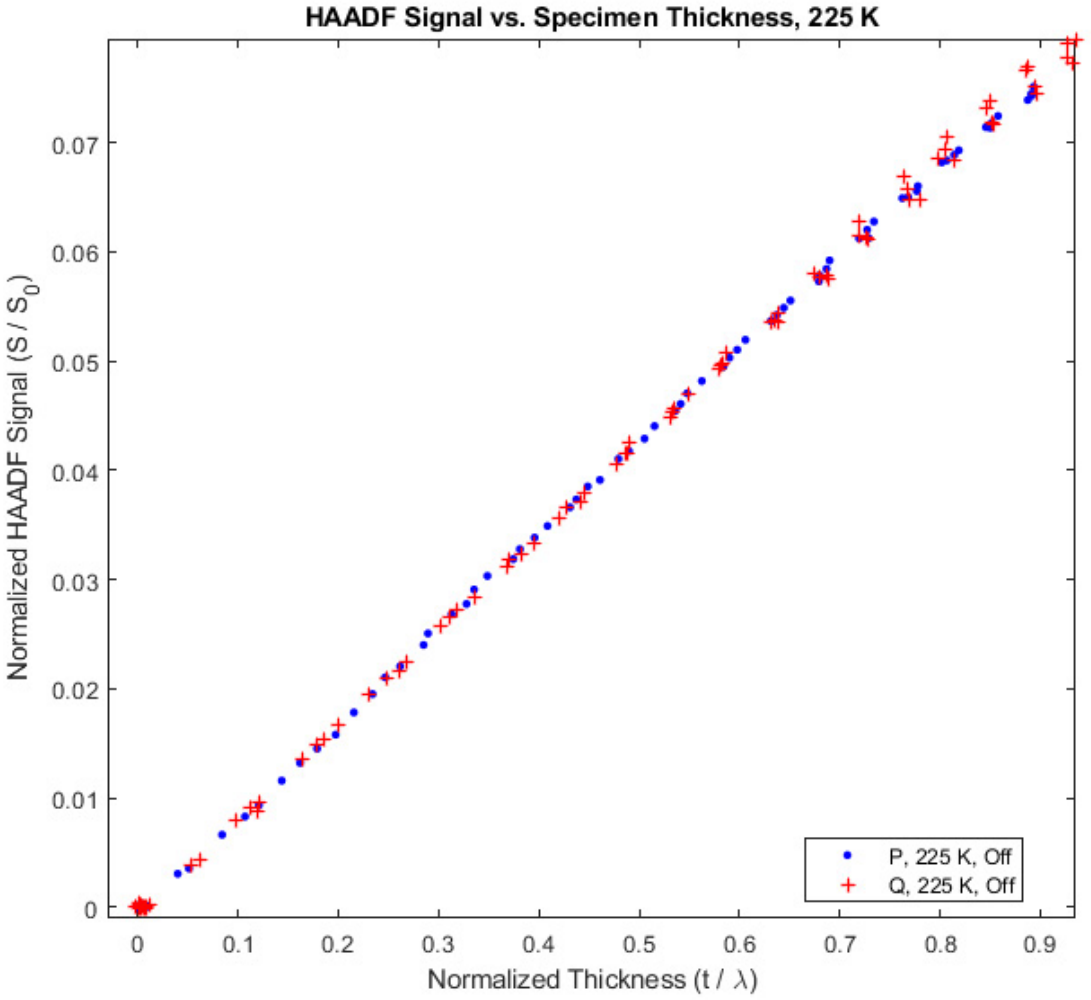

Figure 4-4. Plot of the normalized HAADF signal versus normalized specimen thickness for two maps collected on silicon at 225 K. Once again, the nicely linear data matches the results expected from scattering theory in the thin specimen approximation. [15] The letter in the legend is the experimental run identifier, and 'Off' indicates the data was collected with the sample tilted off-zone.

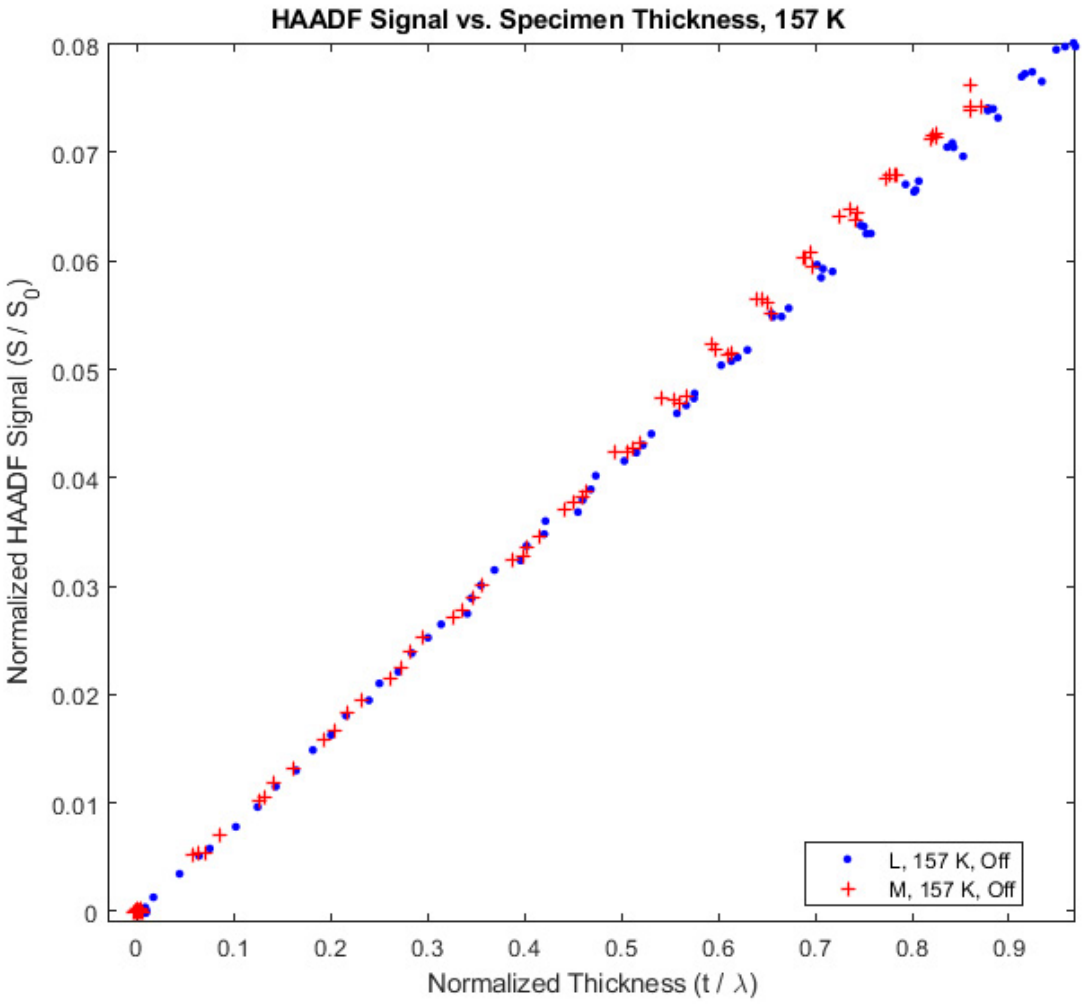

Figure 4-5. Plot of the HAADF signal vs. normalized specimen thickness for two different maps collected on silicon at 157 K. Data is nicely linear up to a thickness of (t / λ) = 0.5. Here, run L (blue dots) diverged slightly from linearity above that thickness, and both get slightly noisier. The cause is unknown, but may be due to a slight shift in the location of CBED spots straddling the edge of the HAADF aperture, an increase in dynamical effects with the higher sample thickness, or both. The letter in the legend is the experimental run, and 'Off' indicates the data was collected with the sample tilted off-zone.

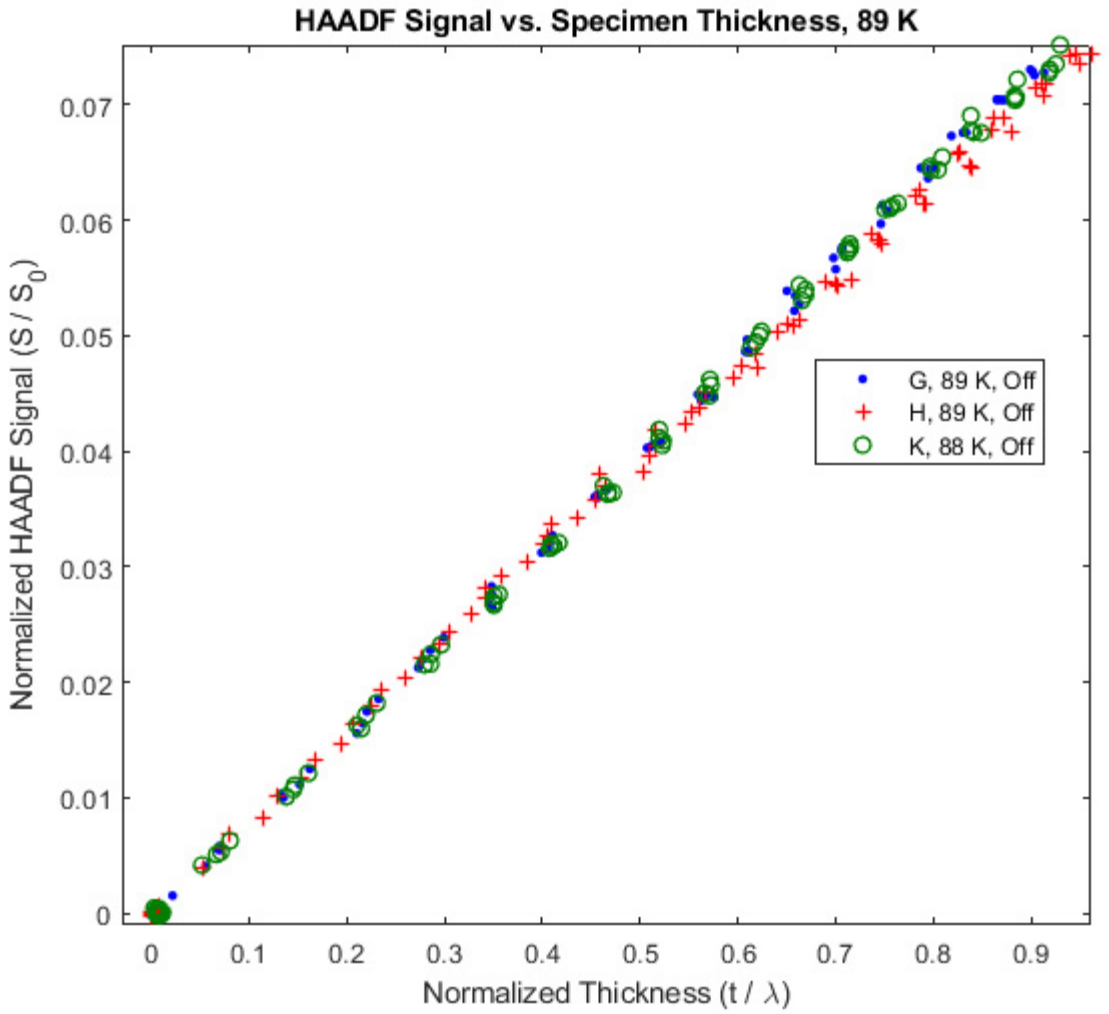

Figure 4-6. Plot of the HAADF signal vs. normalized specimen thickness for three maps collected on silicon at 89 K. As with the 157K data, the runs diverge slightly and get noisier above roughly (t / λ) = 0.5. While the cause is unknown, again the culprit may be a small shift of the CBED direct beam spot in the HAADF aperture, or dynamical scattering effects. The letter in the legend is the experimental run, and 'Off' indicates the data was collected with the sample tilted off-zone.

Figure 4-7 plots $\boldsymbol{S/S_0}$ from three representative runs at 89 K, 157 K, and 225 K. Normalized HAADF signal at a given thickness was seen to increase monotonically with temperature over the experimental temperature range. This reflected the increase in mean atomic vibration amplitude with temperature, and thus the increase in TDS at higher temperature. In Figure 4-8, a plot of a linear fits to the combined data of each temperature demonstrates the small magnitude of the increase in HAADF signal with temperature. The

small change—on the order of 1% of the full beam signal—illustrates the necessity of selecting microscope conditions and HAADF settings favoring high sensitivity and a good signal-to-noise ratio.

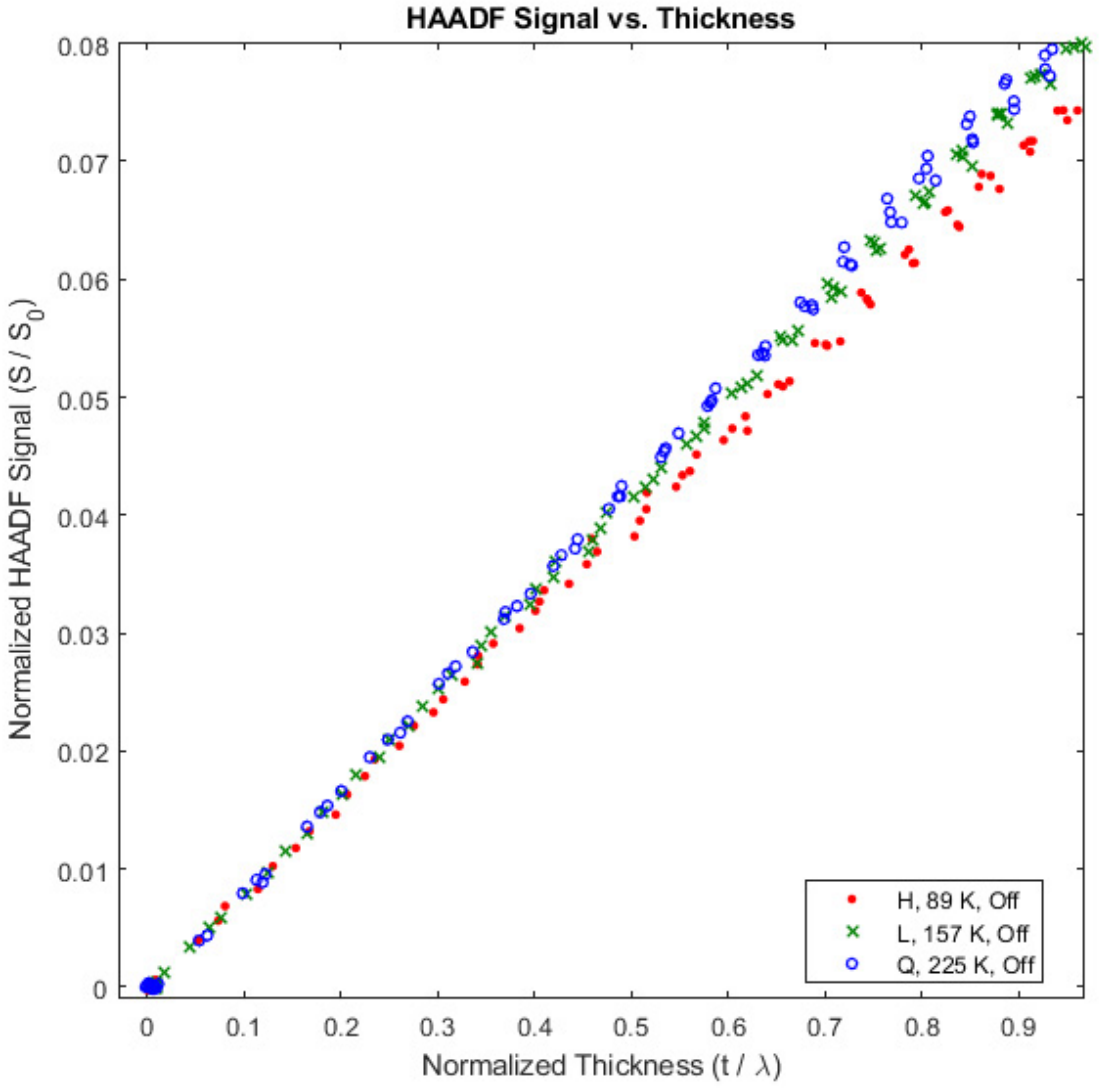

Figure 4-7. HAADF signal versus specimen thickness (both normalized) for three specimen temperatures (89 K, 157 K, 225 K) showing the expected increase in HAADF signal at a given thickness corresponding to increasing TDS with higher temperature. A representative 294 K data set was not included here because it sits so close above the 225 K that it makes the plot difficult to read. See the next figure for a plot of fitted lines including all four experimental temperatures. The letter in the legend is the experimental run, and 'Off' indicates the data was collected with the sample tilted off-zone.

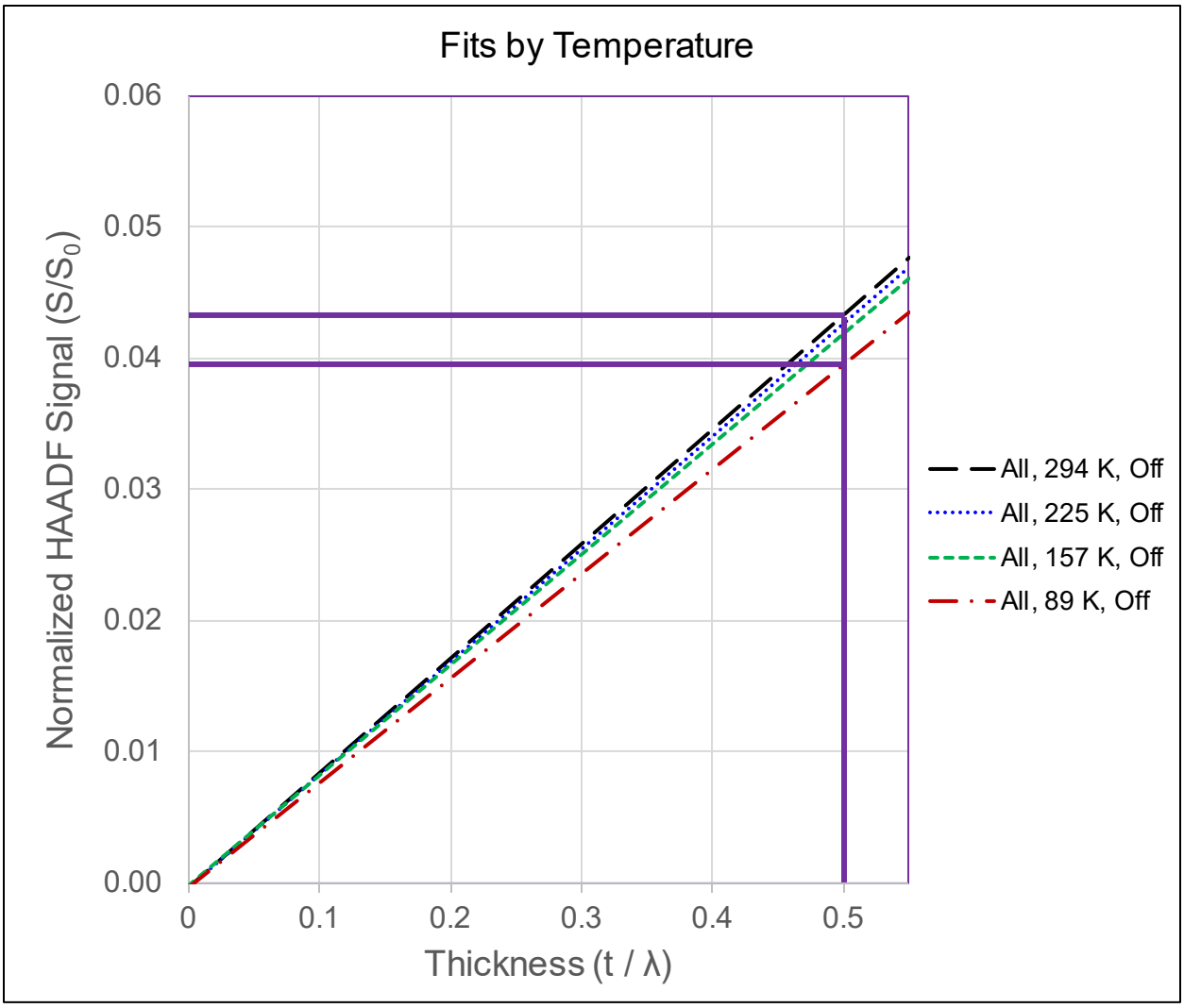

Figure 4-8: Linear fits to collective data set from each temperature. The solid lines show how small the response in HAADF signal is to temperature, even at (t / λ) = 0.5. As previously, the letter in the legend is the experimental run, and 'Off' indicates the data comes from the off-zone tilted sample.

4.3 Obtaining the Temperature Calibration Curve

Combining the results in the range $0 < (t/\lambda) < 0.5$ from the various off-zone maps acquired at different temperatures yielded a plot of the thickness-normalized HAADF signal versus temperature. Fitting a curve to the data produced a curve for HAADF signal versus temperature (see Figure 4-9). The profile of the resulting curve is consistent with the measurements taken on silicon by He and Hull using a broad beam (650nm diameter) and

specimens of uniform thickness: a gradual and slightly non-linear increase in electron scattering with temperature across the range 50 K to 250 K (see Fig. 3a in He and Hull). [11]

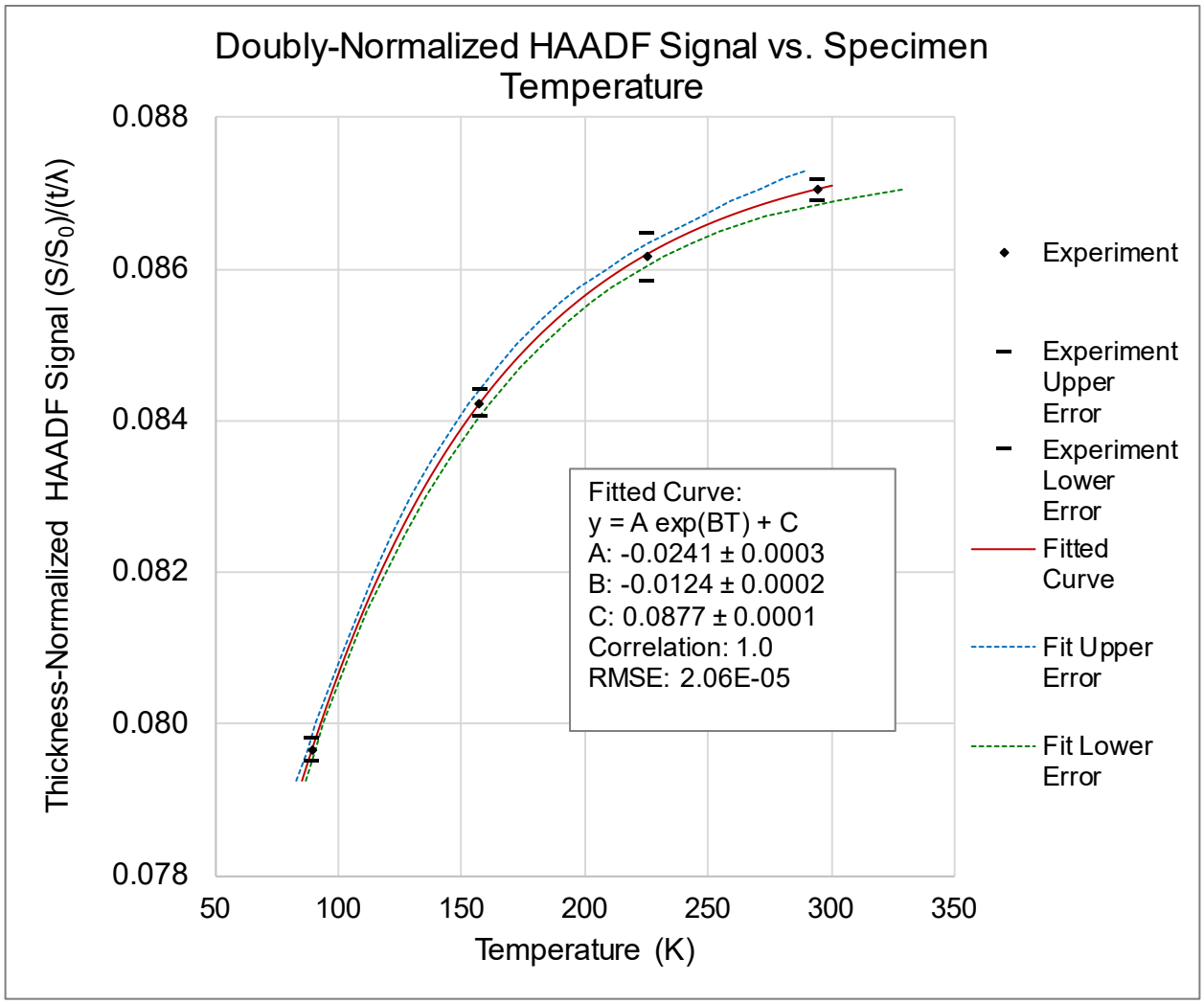

Figure 4-9: Plot of doubly normalized HAADF signal (for full beam and sample thickness) versus specimen temperature for the four experimental temperatures (89 K, 157 K, 225 K, 293 K), with fitted curve. The errors shown are all one standard deviation. The increase in TDS diminishes at higher temperatures for silicon, as seen by other researchers. [11]

The equation obtained for the fitted curve in this experiment took the form

$$\boldsymbol{S}_{norm}/(t/\lambda) = Ae^{BT} + C \tag{4-1}$$

where T is the specimen temperature, A, B, and C are constants, and recalling that $\boldsymbol{S}_{norm}$ is the normalized HAADF signal ($= \boldsymbol{S}/\boldsymbol{S}_0$). The form of the right-hand side of Equation (4-1)

was selected because it provided the best fit from the many linear and non-linear forms that we fitted to the data. This was not surprising, owing to the prevalence of exponential terms in expressions related to thermal phenomena, for example the Debye-Waller factor. For this experiment, A = -0.0241 $\pm$ 0.0003, B = -0.0124 $\pm$ 0.0002, and C = 0.0877 $\pm$ 0.0001. The uncertainty in the constants given above is only the fit uncertainty, and does not incorporate the uncertainty of the measured values for $\boldsymbol{S}_{norm}/(t/\lambda)$. Comparing to Equation (2-16), inspection shows that the calibration constant D is the fit constant A, and $f(T) = e^{BT} + (C/A)$. Solving for temperature T gives an empirically calibrated relationship allowing measurement of local specimen temperature from observations of the HAADF signal and normalized specimen thickness:

$$T = -80.6 \ln(-41.5(\boldsymbol{S}_{norm}/(t/\lambda)) + 3.64) \tag{4-2}$$

The uncertainty of T in Equation (4-2)—as shown graphically in Figure 4-9—was estimated using a Monte Carlo method implemented in a MATLAB script, as described in Appendix A.3. It was not constant, but instead varied with T due to the changing slope of the exponential fit, becoming larger (i.e., more uncertain) as the slope decreased. We estimated the uncertainty in T as $\pm$1.6 K, $\pm$4.3 K, $\pm$7.9 K, and $\pm$29 K, at temperatures of 89 K, 157 K, 225 K, and 294 K, respectively. We note that longer dwell times, acquisitions at more temperatures, and more acquisitions at each temperature could all be employed to reduce the uncertainty in the calibration and in the temperature measurements using that calibration.

Reference dark and bright intensities showed good stability during the many-hour data collection period. Over the 21 runs during 6.5 hours, the bright reference was found to

vary by $\pm$ 0.78% of the detector's dynamic range across all runs. In the same period, the dark reference was found to vary by $\pm$ 0.07% of the detector's dynamic range. While stability over a single day was good, we nevertheless recommend collecting the internal map-specific references to guard against any transients during a day's experimental work in gun emission current, or in the microscope or detector electronics. The HAADF brightness/contrast calibration procedure should be repeated day-to-day or week-to-week, or perhaps more often depending on the observed stability of the microscope used for the measurements.

We did note that the full-beam intensities on the HAADF showed a minor, slow upward drift of approximately 1.0% of the HAADF full dynamic range across the day's experimental runs. We suspect this was due to gradual heating of the HAADF's yttrium aluminum perovskite (YAP) crystal due to repeated exposure to the full beam. We lacked the ability to confirm that through in-situ temperature measurements of the YAP crystal. It could also have been a sensitization of the phosphor, or a long-lifetime excitation. Although the cause was unknown, the observed change was found to be insignificant.

4.4 Measuring the Mean Atomic Vibration Amplitude

Using the off-zone measurements, two-beam single-electron scattering theory can be applied to the results of this experiment to obtain measured values for the mean atomic vibration amplitude $\langle u_s \rangle$ at the experimental temperatures. From Wang, we have the projected radial intensity distribution functions (i.e., the electron intensity at scattering angle θ integrated around the azimuthal angle ϕ) of TDS and elastically scattered electrons. The function for TDS electrons is $2\pi s(f^e)^2(1-e^{-2W})$, and for diffracted (elastically scattered) electrons is $2\pi s(f^e)^2(e^{-2W})$, where s is the scattering vector. $(f^e)^2$ is the square of the atomic electron scattering factor, which is equal to the differential scattering cross

section $d\sigma/d\Omega$. [20,21] W is the Debye-Waller temperature factor, and can be stated in terms of s as $W = 8\pi^2\langle u_s\rangle^2 s^2$. We remind the reader here that the scattering vector s is defined as $s(\theta) = \sin(\theta)/\lambda_B$, where θ is the electron scattering half-angle and λ_B is the wavelength of the beam electrons (0.00251 nm for our 200 keV electrons).

If we define B_m as the scattered TDS electrons measured (i.e, captured) by the HAADF detector, then B_m is obtained by integrating the projected radial intensity distribution between the scattering vectors s_1 and s_2 corresponding to the inner and outer HAADF annulus edges. In these experiments, s_1 was 5.91 nm^{-1} and s_2 was 39.6 nm^{-1}. Defining B_0 as the original beam electrons from which our scattered electrons originated, B_0 is found from the total of the scattered electrons divided by the fraction of beam electrons that undergo a scattering event. From the intensity distributions above, it follows that the total of the scattered electrons is just the integral of $2\pi s(f^e)^2$ over all $s(\theta)$, where θ goes from 0 to π, corresponding to $s(\theta)$ going from 0 nm^{-1} to 398.4 nm^{-1}. Figure 4-10 illustrates these distributions and the scattered electron intensities captured by the HAADF for our experiment at 294 K, showing the dominance of TDS scattered electrons over most of the HAADF's range.

From the definition of the mean free path, the average fraction of scattered electrons from the beam is simply the ratio of specimen thickness to electron mean free path (t/λ). If we neglect the weak contribution of diffracted electrons to the HAADF signal (which the off-zone tilt and camera length were selected to minimize), the measured normalized HAADF

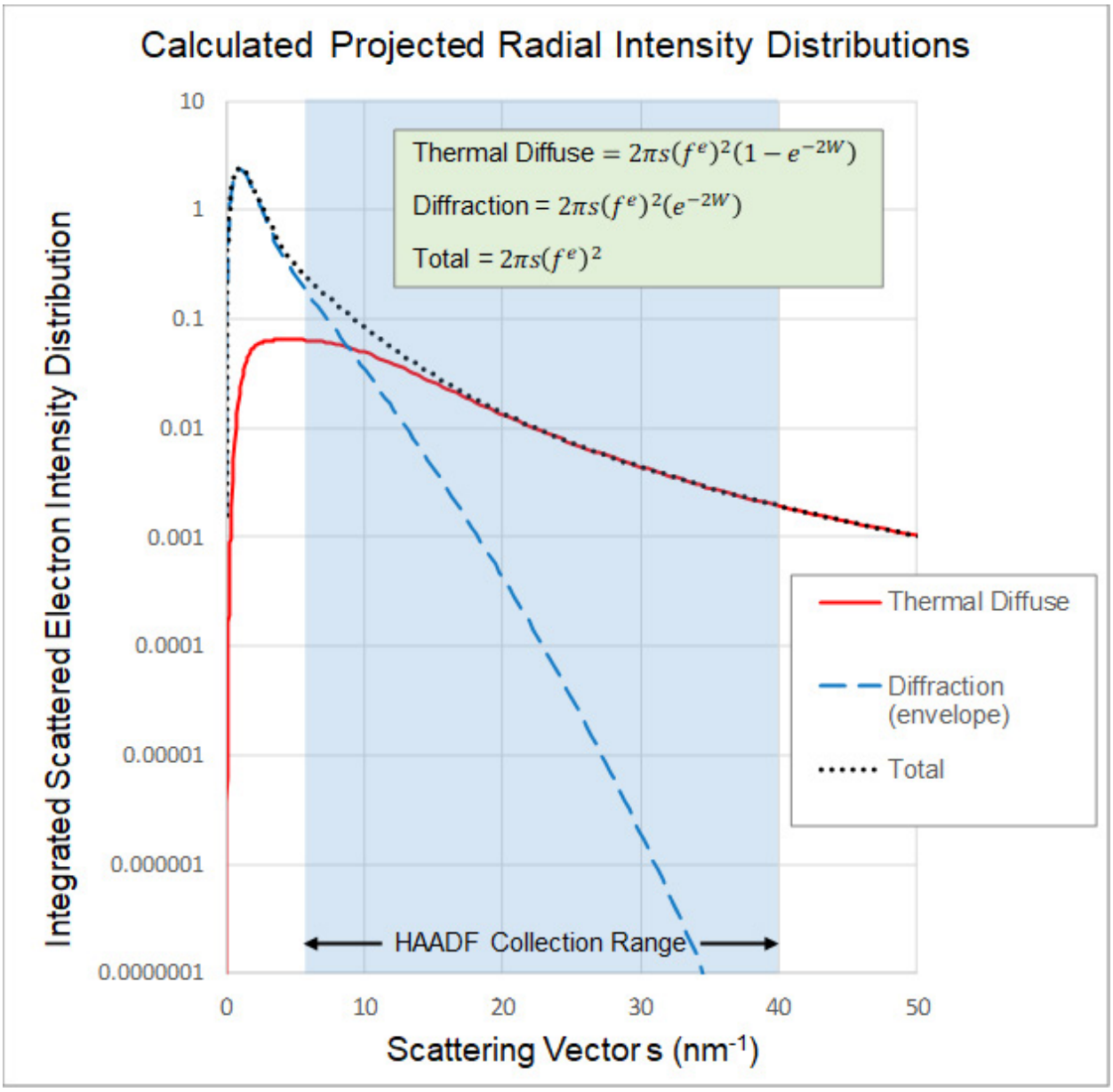

Figure 4-10: Calculated projected radial intensity distributions of scattered electrons from silicon, for a 200 keV beam, using this experiment's measured mean atomic vibration amplitude of 0.00734 nm (i.e, for a room temperature sample). For $(f^e)^2$, the NIST database referred to in the text was used. The diffraction intensity curve is not actually continuously populated, but rather marks the envelope of the intensity of diffraction spots at their specific scattering vectors. The marked range of scattering vectors captured by the HAADF at 200 mm camera length shows how TDS intensity dominates over diffraction intensity across most of the HAADF's range for this microscope condition.

signal $\boldsymbol{S/S_0}$ shown in Figure 4-3 through Figure 4-6 is simply B_m/B_0, and we get an expression relating our measured value to the mean atomic vibration amplitude $\langle u_s \rangle$.

$$\frac{\boldsymbol{S}}{\boldsymbol{S}_0} \approx \frac{B_m}{B_0} = (t/\lambda)\left(\frac{\int_{s_1}^{s_2} 2\pi s (f^e)^2 \left(1 - e^{-16\pi^2 \langle u_s \rangle^2 s^2}\right) ds}{\int_{s(0)}^{s(\pi)} 2\pi s (f^e)^2 ds}\right)$$

(4-3)

The appropriate differential scattering cross section to use as f^e for TDS electrons and the elastically scattered (i.e., diffracted) electrons is the differential elastic scattering cross section, which NIST has tabulated for silicon. [13,22]

Fitting lines to the room temperature data (294 K) in Figure 4-3 gives a mean value of the slope of $(\boldsymbol{S}/\boldsymbol{S}_0)/(t/\lambda) = 0.08705$, and so $\boldsymbol{S}/\boldsymbol{S}_0$=0.04353 when (t/λ) is 0.5. Numerical integration of the integrals in Equation (4-3), using linear interpolation between the measured points in the NIST database, reveals that to produce that value of $\boldsymbol{S}/\boldsymbol{S}_0$ when $(t/\lambda) = 0.5$ requires $\langle u_s \rangle$ to be 0.00738 +/- 0.00002 nm. This value is in reasonable agreement with Aldred and Hart's value of 0.00755 nm measured using X-rays. [23] Doing the same calculation for the data taken around 89 K in Figure 4-6 gives a value for $\langle u_s \rangle$ of 0.00674 +/- 0.00002 nm. This is considerably higher than Aldred and Hart's X-ray measurement of 0.00536 nm. The errors in $\langle u_s \rangle$ were estimated by using the upper and lower deviations of S/S_0 for each case, determining $\langle u_s \rangle$ from each, then taking the larger difference between the measured value and the error values as the estimated error.

The difference in the 89 K value as compared to Aldred and Hart is an expected artifact of the model used. The expressions used in Equation (4-3) were derived from the Einstein model, which treats atoms as independent harmonic oscillators and takes no account of the low frequency phonons that contribute substantially to the atomic displacement at low temperatures. [14] Consequently, at low temperatures it under-predicts the amount of TDS relative to the beam (i.e., it under-predicts the value of $\boldsymbol{S}/\boldsymbol{S}_0$), and for a

measured low-temperature value of S/S_0 it over-predicts the mean atomic vibration amplitude needed to produce that amount of TDS.

4.5 A Tool for Testing Electron Scattering Models

A slight rearrangement of Equation

(4-3) produces the following notable expression:

$$\frac{\boldsymbol{S/S_0}}{(t/\lambda)} = \left(\frac{\int_{s_1}^{s_2} 2\pi s (f^e)^2 \left(1 - e^{-16\pi^2 \langle u_s \rangle^2 s^2}\right) ds}{\int_{s(0)}^{s(\pi)} 2\pi s (f^e)^2 ds} \right) \tag{4-4}$$

The left side of Equation (4-4) is composed solely of empirical measurements. The right side is entirely expressions from a theory-based model. This offers the promising potential that the method presented here can be adapted to test models for which the model parameters are known or can be obtained. A simple example would be to use the previously employed NIST Electron Elastic-Scattering Cross-Section Database with the same model to make measurements of $\langle u_s \rangle$ for other solid elements, for comparison with values obtained from X-rays and neutron scattering. Measure of mean atomic vibration amplitudes for as-yet-unmeasured elements could be done. Substituting in a scattering model for a multi-element material would allow testing of that model on compounds like oxides, for example, and might allow measurement of local specimen composition. Substitution of a scattering model for amorphous solids, in turn, would permit testing of that model against glassy solids.

It is also worth observing that the left side of Equation (4-4) does not have microscope parameters as explicit inputs. This suggests the method should be relatively easily portable to other STEM-capable microscopes equipped with a HAADF and EELS.

4.6 On-Zone Scattered Electron Signal vs. Thickness

During experimentation, as indicated previously, data was also acquired with the specimen tilted to align the beam to a low index zone (the [001] zone). Analysis of the data found that the presence of a number of strongly excited diffraction spots straddling the inner edge of the HAADF made the results extremely sensitive to the pattern alignment in the HAADF aperture and to microscope beam alignment (specifically to the beam tilt pivot points). This was because any deviation in alignment produced a slight CBED pattern shift on the HAADF during scanning, causing excessive variability in the HAADF signal collected. A search for compatible on-zone microscope conditions was not attempted. Comparison between data from a run collected off-zone and runs collected on zone is shown for room temperature in Figure 4-11, and for near liquid nitrogen temperature in Figure 4-12. To make on-zone measurement practical, a set of microscope conditions would need to be identified that reduces or eliminates this sensitivity while still satisfying the requirements for signal-to-noise and avoidance of detector saturation.

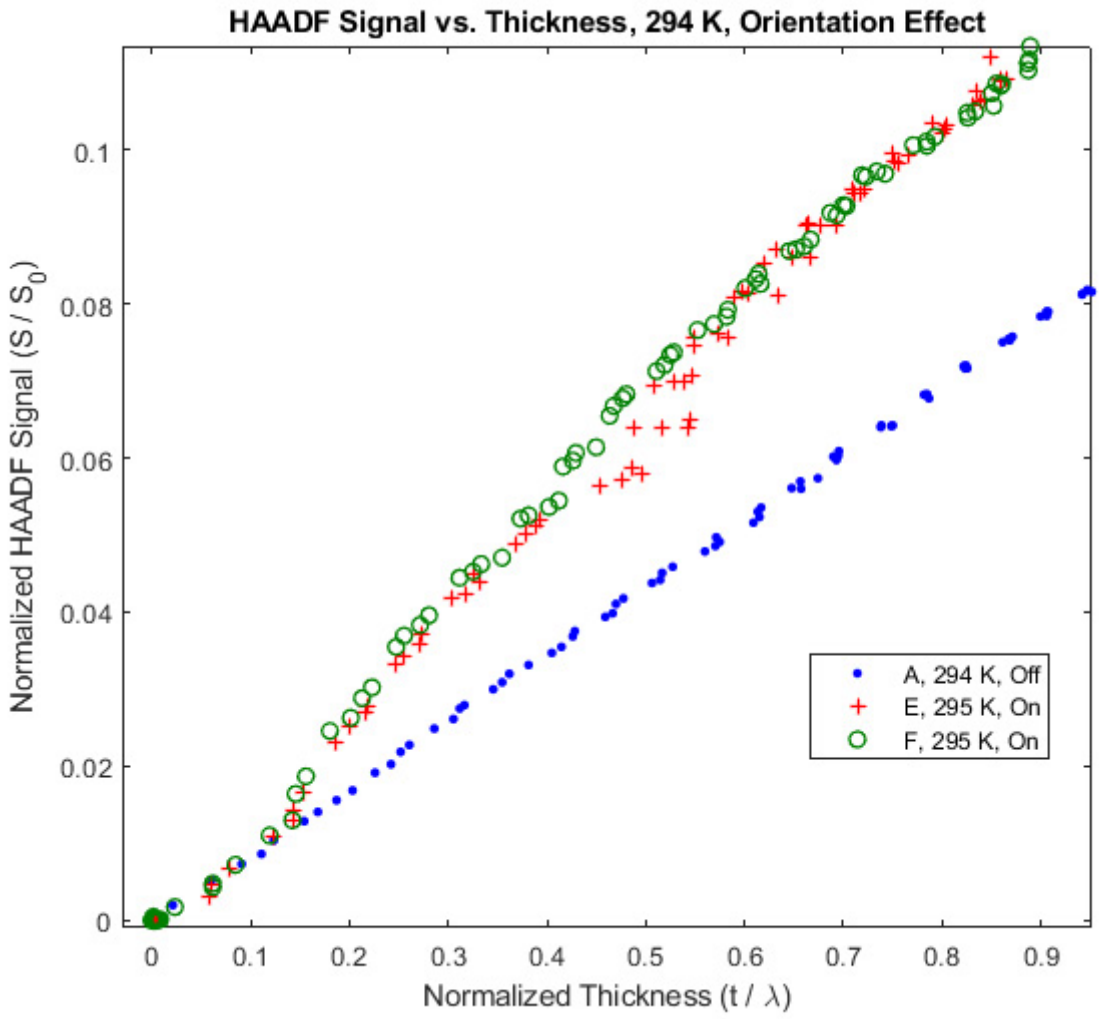

Figure 4-11. Plot of the HAADF signal (normalized to the full beam signal) versus specimen thickness (normalized to the mean free path of the beam electrons as measured using EELS spectra) for off-zone run A, and on-zone runs E and F at room temperature. All three datasets overlay nicely up to a normalized thickness of approximately 0.15, but then the on-zone runs diverge non-linearly upward, showing increased HAADF signal relative to the expected linear signal. The letter in the legend is the experimental run; 'Off' indicates the data was collected with the sample tilted off-zone; and 'On' indicates the data was collected with the sample oriented on the [001] zone.

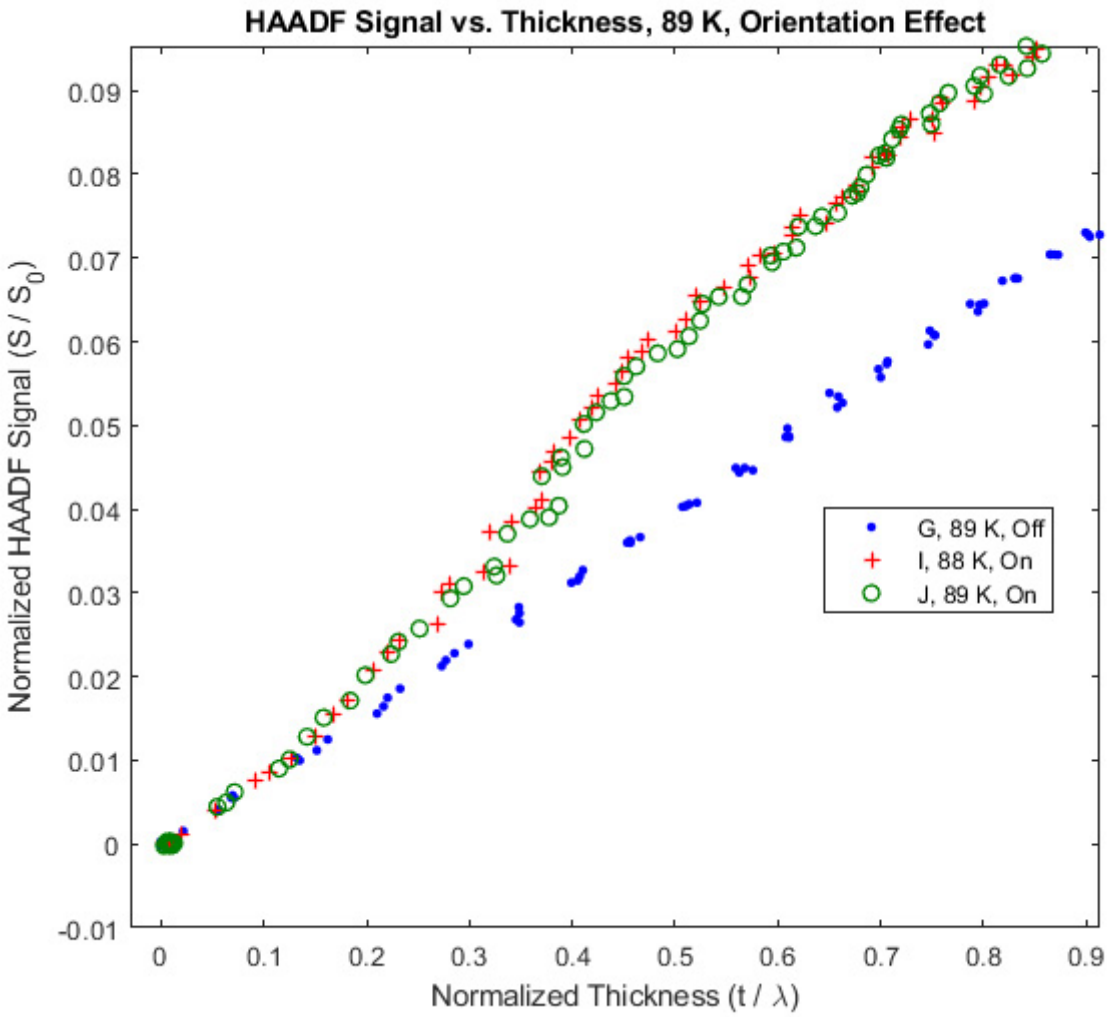

Figure 4-12. Plot of the HAADF signal (normalized to the full beam signal) versus specimen thickness (normalized to the mean free path of the beam electrons as measured using EELS spectra) for off-zone run G, and on-zone runs I and J at 89 K. Once again, all three datasets overlay nicely up to around a normalized thickness of 0.15, but then the on-zone runs diverge upward, showing increased HAADF signal relative to the expected linear signal. Like the previous figure, the letter in the legend is the experimental run; 'Off' indicates the data was taken with the specimen oriented off-zone; and 'On' indicates the data was collected with the sample on the [001] zone.

5 Conclusion

We have developed a method for measuring the effects of specimen temperature and thickness on thermal diffuse scattering using unmodified, off-the-shelf equipment: a STEM with conventional HAADF and EELS system. $\boldsymbol{S}/\boldsymbol{S}_0$ and (t/λ) can be extracted and analyzed to yield a material-specific calibration curve allowing high-spatial-resolution in-situ temperature measurements on specimens of that material which have locally varying thicknesses. Additionally, it offers the ability to make a quantitative indirect measurement of the atomic vibration amplitude versus temperature for materials near room temperature or higher, and has demonstrated potential for as a tool for quantitative testing of electron scattering models.

Possibilities for future work are extensive. Testing of electron scattering models is of particular interest. This could include finding microscope settings and conditions to allow successful measurements on-zone for low index zones of silicon or other crystalline materials; identifying and testing a scattering model designed for lower specimen temperatures; adapting the technique to test models for measuring an amorphous material such as silicon dioxide; determining microscope parameters for analyzing and taking mean atomic vibration amplitude measurements for other elemental solids, particularly ones as yet unmeasured in the literature; and attempting to adapt the technique to detect compositional changes in a specimen while accounting for thickness and temperature. Additionally, automating the data acquisition on the microscope could be done, or perhaps further automation of the post-processing would be fruitful.

6 References

[1] J.M. LeBeau, S. Stemmer, Experimental quantification of annular dark-field images in scanning transmission electron microscopy, Ultramicroscopy. 108 (2008) 1653–1658. https://doi.org/10.1016/j.ultramic.2008.07.001.

[2] J.Y. Zhang, J. Hwang, B.J. Isaac, S. Stemmer, Variable-angle high-angle annular dark-field imaging: application to three-dimensional dopant atom profiling, Sci Rep. 5 (2015) 12419. https://doi.org/10.1038/srep12419.

[3] X. Jiang, M. Jiang, M. Zhao, Shape effect on the size and dimension dependent order–disorder transition temperatures of bimetallic alloys, Physica B: Condensed Matter. 406 (2011) 4544–4546. https://doi.org/10.1016/j.physb.2011.08.093.

[4] D.A. Muller, L.F. Kourkoutis, M. Murfitt, J.H. Song, H.Y. Hwang, J. Silcox, N. Dellby, O.L. Krivanek, Atomic-Scale Chemical Imaging of Composition and Bonding by Aberration-Corrected Microscopy, Science. 319 (2008) 1073–1076. https://doi.org/10.1126/science.1148820.

[5] B.D. Esser, A.J. Hauser, R.E.A. Williams, L.J. Allen, P.M. Woodward, F.Y. Yang, D.W. McComb, Quantitative STEM Imaging of Order-Disorder Phenomena in Double Perovskite Thin Films, Phys. Rev. Lett. 117 (2016) 176101. https://doi.org/10.1103/PhysRevLett.117.176101.

[6] R.V. Petrova, R.R. Vanfleet, D. Richardson, Bo Yao, K.R. Coffey, Characterization of individual L1/sub 0/ FePt nanoparticles, IEEE Transactions on Magnetics. 41 (2005) 3202–3204. https://doi.org/10.1109/TMAG.2005.855267.

[7] L. Jones, Quantitative ADF STEM: acquisition, analysis and interpretation, IOP Conf. Ser.: Mater. Sci. Eng. 109 (2016) 012008. https://doi.org/10.1088/1757-899X/109/1/012008.

[8] J. Christofferson, K. Maize, Y. Ezzahri, J. Shabani, X. Wang, A. Shakouri, Microscale and Nanoscale Thermal Characterization Techniques, Journal of Electronic Packaging. 130 (2008). https://doi.org/10.1115/1.2993145.

[9] R. Egoavil, N. Gauquelin, G.T. Martinez, S. Van Aert, G. Van Tendeloo, J. Verbeeck, Atomic resolution mapping of phonon excitations in STEM-EELS experiments, Ultramicroscopy. 147 (2014) 1–7. https://doi.org/10.1016/j.ultramic.2014.04.011.

[10] J.C. Idrobo, A.R. Lupini, T. Feng, R.R. Unocic, F.S. Walden, D.S. Gardiner, T.C. Lovejoy, N. Dellby, S.T. Pantelides, O.L. Krivanek, Temperature Measurement by a Nanoscale Electron Probe Using Energy Gain and Loss Spectroscopy, Phys. Rev. Lett. 120 (2018) 095901. https://doi.org/10.1103/PhysRevLett.120.095901.

[11] L. He, R. Hull, Quantification of electron–phonon scattering for determination of temperature variations at high spatial resolution in the transmission electron microscope, Nanotechnology. 23 (2012) 205705. https://doi.org/10.1088/0957-4484/23/20/205705.

[12] G. Wehmeyer, K.C. Bustillo, A.M. Minor, C. Dames, Measuring temperature-dependent thermal diffuse scattering using scanning transmission electron microscopy, Applied Physics Letters. 113 (2018) 253101. https://doi.org/10.1063/1.5066111.

[13] C.R. Hall, The scattering of high energy electrons by the thermal vibrations of crystals, Philosophical Magazine. 12 (1965) 815–826. https://doi.org/10.1080/14786436508218919.
[16] Z.L. Wang, Elastic and inelastic scattering in electron diffraction and imaging, Plenum Press, New York, 1995, p. 194.
[14] R.F. Egerton, Electron energy-loss spectroscopy in the electron microscope, 2nd ed, Plenum Press, New York, 1996, pp. 186-187, 302-303.
[15] Z.L. Wang, Elastic and inelastic scattering in electron diffraction and imaging, Plenum Press, New York, 1995, p. 222.
[17] Fischione Instruments Model 3000 Annular Dark Field (ADF) Detector Instruction Manual, E. A. Fischione Instruments, Inc., Export, PA 15632, 2000.
[18] E.J. Kirkland, M.G. Thomas, A high efficiency annular dark field detector for STEM, Ultramicroscopy. 62 (1996) 79–88. https://doi.org/10.1016/0304-3991(95)00092-5.
[19] C.C. Ahn, O.L. Krivanek, EELS Atlas, Gatan Inc., Warrendale, PA 15086, 1983.
[17] Z.L. Wang, Elastic and inelastic scattering in electron diffraction and imaging, Plenum Press, New York, 1995, p. 195.
[21] D.B. Williams, C.B. Carter, Transmission electron microscopy: a textbook for materials science, 2. ed, Springer, New York, 2009.
[22] A. Jablonski, F. Salvat, C. J. Powell, A. Y. Lee, NIST Electron Elastic-Scattering Cross-Section Database Version 4.0, NIST Standard Reference Database Number 64, National Institute of Standards and Technology, Gaithersburg MD, 20899, 2016. https://srdata.nist.gov/srd64/ (accessed August 2, 2021).
[23] P.J.E. Aldred, M. Hart, The electron distribution in silicon - II. Theoretical interpretation, Proc. R. Soc. Lond. A. 332 (1973) 239–254. https://doi.org/10.1098/rspa.1973.0023.

Appendix A The MATLAB Scripts

A.1. The Map Script

This is the script used to process the maps collected. It was run using MATLAB version R2019a. It is a heavily modified version of a script originally created by Richard Vanfleet and Rumyana Petrova.

When run, the script opens a file dialog box for the user to select one or more .emi files to be processed. The script expects to find two additional files to be in the same folder for each .emi file and any associated .ser files, as explained below. Both files must be present for the script to execute correctly. Modification of the script would be required to omit either one or both.

The first file is the HAADF detector image from the map which has been exported as a RAW file type in Tecnai Imaging and Analysis (TIA), and given the same name as the .emi file, but it will have the extension .bin. This is where the script gets the unmodified HAADF signal values for each pixel. The HAADF values on the microscope used in the experiment ranged from 0 to 65520.

The second file is a text file containing the dark and bright reference HAADF values from the map in the .emi file. It contains only two numbers separated by a space, with the first number being the dark reference HAADF value for that map, obtained by using the 'Statistics' functionality in TIA to select and average the HAADF signals of the map pixels where the beam was off the sample (recommend at least 12 pixels, 16 is better if available in the map). The second number is the bright reference HAADF value from the map, computed

again using the 'Statistics' functionality in TIA by averaging the rightmost 2-3 pixels of the map's final row.

In the script below, green text is comments (these are preceded by a percent character). Some statements have been commented out. One reason was statements that are optional—they can be enabled but will slow the execution down dramatically during processing of files. A few commented-out statements are old predecessors of some of the modifications. These were retained as comments in case it became necessary to revert to the non-modified version of the script.

The rest of the text is code, with the coloration assigned by the MATLAB editor to indicate the type of information (strings, numbers, commands, etc.).

A.2. The Map Script Code

```
%Routine to format TIA data files, EELS data for statistical analysis
%filebase is the name of the emi data file.  the eels data is kept in the
%filename_1.ser file.  Also, the ADF part of the data (the HAADF image part
of the map) should be exported as
%a filename.bin file (a RAW file type in TIA) prior to using this script.
%File names must not include other periods except to mark the extension!
%Script assumes user has measured HAADF min and max values (zero and full
%beam signal levels)--min from the collected HAADF portion of the map, and
%max from the last two rows of the map which are ignored for data analysis

%Initialization
clear
%haadfmax=65520; %The max signal level for full beam on the haadf for this
dataset from a reference image.
%haadfmin=35; %The min signal level on the haadf for this dataset from a
reference image.
showProgress=false; %display processing progress by putting border on each
finished pixel
showSpectra=false; %display fit and ZLP-calibrated spectrum for current
spectrum being processed
global num_spec specdata
% normal color sequence
colorPalette = [
    [0 0.4470 0.7410]; % medium blue
    [0.8500 0.3250 0.0980]; % medium brown
    [0.9290 0.6940 0.1250]; % light orange
    [0.4940 0.1840 0.5560]; % purple
    [0.4660 0.6740 0.1880]; % medium green
```

```
    [0.3010 0.7450 0.9330]; % light blue
    [0.6350 0.0780 0.1840]; % dark brown
    [1 0 0]; % bright red
    [0 1 0]; % bright green
    [0 0 1]; % bright blue
    [1 1 0]; % bright yellow
    [0 1 1]; % bright cyan
    [1 0 1]; % bright magenta
    ];

%Get the list of files to process
fileList={};
[fileList, pathName] = uigetfile('*.bin', 'Select the files you wish to
process (only ones listed are those that have .bin
images)','MultiSelect','on');
%How many files were selected?
if isa(fileList,'char')
    disp("one file selected")
    fileCount = 1;
    fileList = cellstr(fileList); %if one file was selected, convert returned
char vector to cell so array indexing works correctly on fileList
elseif isa(fileList,'cell')
    disp("multiple files selected")
    fileCount = size(fileList,2);
end %if isa fileList
%initialize data labels for plot legends
dataLegend = strings(1,fileCount);

%create the figures
fig1 = figure('Position',[605 671 560 420]); %this shows spectrum and fit for
monitoring and debugging
fig2 = figure('Position',[1200 671 560 420]); %this plots cumulative results
set(groot,'defaultAxesColorOrder',colorPalette)


%Process selected files sequentially and save results for each one as we go
for currentFile = 1:1:fileCount
    t0=clock;
    fileName=split(fileList(currentFile),".");
    fileBase=fileName(1,1);
    cd(pathName);

    sourceFile=fileBase+"_1.ser"; % the _1.ser files holds the spectra
    adfFile=fileBase+".bin";
    refFile=fileBase+".txt";

    dataLegend(currentFile)=fileBase{1}(1:2); %set the legend as the first 3
characters of the filename
    pause(1)

    %Pull white and black level from text file
    fid=fopen(refFile,'r');
    haadfref=fscanf(fid,'%d %d',2);
    haadfmin=haadfref(1)
    haadfmax=haadfref(2)
```

```
    ST=fclose(fid);

    %Open adf data file
    fid=fopen(adfFile,'r');
    RawData=fread(fid,200000,'uchar');
    datafmt=(RawData(1)+(RawData(2)*256));
    if datafmt==7
       fmt='single';
    elseif datafmt==2
        fmt='uint16';
    else
        disp ('format error in data type assumed not what is reported in file
')
    end


Nw=(RawData(3)+(RawData(4)*256)+(RawData(5)*65536)+(RawData(6)*16777216));

Nh=(RawData(7)+(RawData(8)*256)+(RawData(9)*65536)+(RawData(10)*16777216));
    %imdata=zeros(Nw,Nh);

   Offset=10;

    %First fseek sets file position to the start of the data

    status=fseek(fid,Offset,'bof');

    imdata=(fread(fid,[Nw Nh],fmt))';

    ST=fclose(fid);

    % The image data has now been read into imdata

    %Open spectra data file
    fid=fopen(sourceFile,'r');
    RawData=fread(fid,200000,'uchar');

num_spec=(RawData(15)+(RawData(16)*256)+(RawData(17)*65536)+(RawData(18)*1677
7216)); %number of spectra or images in file
    Offset=(RawData(23))+1;

OffsetArrayOffset=(RawData(Offset)+(RawData(Offset+1)*256)+(RawData(Offset+2)
*65536)+...
        (RawData(Offset+3)*16777216)); %start of first spectra data

    Spec_Data_type=RawData(OffsetArrayOffset + 21);

nchannels=RawData(OffsetArrayOffset+23)+(RawData(OffsetArrayOffset+24)*256);
% number of elements in each spectrum
    %Preallocate X matrix
    specdata=zeros(num_spec, nchannels);

    %Read in data. Output is (num_spec, channels)
    %26 bytes spectrum header)
```

```
    %First fseek sets file position to the start of the first spectrum, first
file header (26bytes) +
    status=fseek(fid,(OffsetArrayOffset),'bof');

    for i=1:num_spec
        oset(i)=fread(fid,1,'double'); %offset of calibration element (cele)
ie, pixel cele is offset by oset amount
        delta(i)=fread(fid,1,'double'); % scale, energy step per pixel
        cele(i)=fread(fid,1,'int32'); % see oset
        dt(i)=fread(fid,1,'int16'); % time step between spectra?
        al(i)=fread(fid,1,'int32'); %size of spectrum?
        specdata(i,:)=(fread(fid,nchannels,'int32'))';
        %read tags (time and position)
        %Second fseek increments the file position to the start of the next
spectrum 26 bytes
        %spectrum's header
        a(i)=fread(fid,1,'int32'); %a,b,x,y are positions of data points
        b(i)=fread(fid,1,'int32');  %a,b are within the array (line is
unchanged in one direction)
        x(i)=fread(fid,1,'double');  %x,y are positions of points relative to
center of image (unit seems to be um)
        y(i)=fread(fid,1,'double');
    end %for i

    ST=fclose(fid);
    %specdata(i,j) now holds all the EELS spectra.  first index is the number
of the spectra and the
    %second index is the spectra itself.  header data are in vectors
    %oset,....a,b,x,y


    %outarray=[num_spec nchannels delta(1) oset(1) cele(1)];
    channels = 1 : 1 : nchannels; % Create a vector of length = number of
channels(points in the spectrum)

    specx=channels*delta(1)+oset(1);  %this is the energy scale for the
spectra
    xaxis=[min(x) max(x)]; % x range of positions for the spectra
    yaxis=[min(y) max(y)]; % y range of position for the spectra

    xx=round((Nw-1)*(x-xaxis(1))/(xaxis(2)-xaxis(1)))+1; %xx, yy become
pointers to the integer position of each spectra
                        % ie xx(3) is the x position in steps of spectra 3
    yy=Nh-round((Nh-1)*(y-yaxis(1))/(yaxis(2)-yaxis(1)));

    y=max(y)+min(y)-y;

    dx=(xaxis(2)-xaxis(1))/(Nw-1);
    dy=(yaxis(2)-yaxis(1))/(Nh-1);

    figure(fig1);
    clf(fig1)
    fig1.Name=char(fileBase);

    subplot(2,1,1)
```

```
    h=imagesc(xaxis,yaxis,imdata);
    hold on

    alpha=[1 1 1 1 1 1 1 1 1 1
         1 1 0 0 0 0 0 0 1 1
         1 1 0 0 0 0 0 0 1 1
         1 1 0 0 0 0 0 0 1 1
         1 1 0 0 0 0 0 0 1 1
         1 1 1 1 1 1 1 1 1 1];

    tempimage=imdata;
    adfval=imdata;

    %Predefine variable sizes to speed up execution
    t1=zeros(Nh,Nw,'double');
    t2=zeros(Nh,Nw,'double');
    I0=zeros(Nh,Nw,'double');
    Iin=zeros(Nh,Nw,'double');
    a1=zeros(Nh,Nw,'double');
    b1=zeros(Nh,Nw,'double');
    c1=zeros(Nh,Nw,'double');
    a2=zeros(15,60,'double');  %only need if using gauss2 fit below
    b2=zeros(15,60,'double');  %only need if using gauss2 fit below
    c2=zeros(15,60,'double');  %only need if using gauss2 fit below
    %a3=zeros(15,60,'double');  %only need if using gauss3 fit below
    %b3=zeros(15,60,'double');  %only need if using gauss3 fit below
    %c3=zeros(15,60,'double');  %only need if using gauss3 fit below
    %a4=zeros(15,60,'double');  %only need if using gauss4 fit below
    %b4=zeros(15,60,'double');  %only need if using gauss4 fit below
    %c4=zeros(15,60,'double');  %only need if using gauss4 fit below
    %gr=zeros(Nh,Nw,'double');  %only need if looking fit's r-squared
    specxCalZLP=zeros(1,nchannels,'double');

    for i=1:(4*Nw) %process first 4 rows, ignore subsequent rows where bright
reference is
        [f, g]=fit(specx',specdata(i,:)','gauss2');  %fit the EELS spectra
with gaussian(s)
        a1(yy(i),xx(i))=f.a1;  %fit parameter for each gaussian
        b1(yy(i),xx(i))=f.b1;  %all these t1, t2, a1, b1, ... are NxM
matrices with index matching the position in x,y of the data point
        c1(yy(i),xx(i))=f.c1;
        a2(yy(i),xx(i))=f.a2;  %only needed for a gauss2 fit
        b2(yy(i),xx(i))=f.b2;  %only needed for a gauss2 fit
        c2(yy(i),xx(i))=f.c2;  %only needed for a gauss2 fit
    %    a3(yy(i),xx(i))=f.a3; %only needed for a gauss3 fit
    %    b3(yy(i),xx(i))=f.b3; %only needed for a gauss3 fit
    %    c3(yy(i),xx(i))=f.c3; %only needed for a gauss3 fit
    %    a4(yy(i),xx(i))=f.a4; %only needed for a gauss4 fit
    %    b4(yy(i),xx(i))=f.b4; %only needed for a gauss4 fit
    %    c4(yy(i),xx(i))=f.c4; %only needed for a gauss4 fit
    %    gr(yy(i),xx(i))=g.rsquare; %only needed for fit's r-squared
        specxCalZLP=specx-b1(yy(i),xx(i)); %calibrate spectrum energy using
zero loss peak center as offset
        I0(yy(i),xx(i))=sum(specdata(i,((specxCalZLP<=3) & (specxCalZLP>=-
3))));  %sum the spectra for points when Energy is less than the given value
(3 eV)
```

```
        Iin(yy(i),xx(i))=sum(specdata(i,specxCalZLP>3));  %sum the inelastic
scattered spectra for points greater than the given value (3 eV)
        if showSpectra %displays spectra as it processes them for
understanding data
            figure(fig1)
            subplot(2,1,2)
            plot(f,specxCalZLP,specdata(i,:)) %plots fit as curve and ZLP-
calibrated spectrum as points
            %plot(specx,specdata(i,:))  %plots original unadjusted spectrum
            %plot(f,specx,specdata(i,:)) %plots fit as curve and original
unadjusted spectrum as points
        end %if showSpectra
        if showProgress %highlights current pixel of map being processed
            figure(fig1)
            subplot(2,1,1)
            h=image(max(max(imdata))*alpha,'Xdata',[x(i)-dx/2
x(i)+dx/2],'Ydata',[y(i)-dy/2 y(i)+dy/2]);
            set(h,'AlphaData',alpha);
        end %if showProgress
    end %for i, computing inelastically scattered and unscattered intensities
    %scale ADF intensities to range of zero-to-full beam
    adfval2=(adfval-haadfmin)/(haadfmax-haadfmin);
    %compute HAADF intensity vs t/lambda
    for row=1:1:Nh
        for col=1:1:Nw
            haadfIntensity((row-1)*Nw+col,currentFile)=adfval2(row,col);
            tlambda((row-
1)*Nw+col,currentFile)=log(1+(Iin(row,col)/I0(row,col)));
        end %for col
    end %for row

    figure(fig2)
    cla(fig2)
%
plot(log(1+(Iin./I0)),adfval2+0.05,'LineStyle','none','Marker','.','Color',
...
%        [colorPalette(currentFile+7,1) colorPalette(currentFile+7,2)
colorPalette(currentFile+7,3)])
%
plot(tlambda(currentFile,:),haadfIntensity(currentFile,:),'LineStyle','none',
'Marker','.','Color', ...
%         [colorPalette(currentFile,1) colorPalette(currentFile,2)
colorPalette(currentFile,3)]);

plot(tlambda,haadfIntensity,'LineStyle','none','Marker','.','MarkerSize',10);
    legend(dataLegend(1:currentFile),'Location','northeastoutside');
    axis([-0.1 inf -0.01 inf])
    ylabel("Normalized HAADF Intensity")
    xlabel("t / lambda")
    title(fileBase)
    %Compute elapsed clock time to run this routine
    disp ('Elapsed clock time (minutes) to run routine is ')
    (etime(clock,t0))/60
end %for currentFile
figure(fig2)
```

```
%save the computed dataset
outFilename="";
outFilename = strcat(strjoin(deblank(dataLegend))," results.mat")
save(outFilename,'fileCount', 'fileList', 'dataLegend', 'tlambda',
'haadfIntensity')
ExcelFilename = strcat(strjoin(deblank(dataLegend))," results.xls")
xlswrite(ExcelFilename,dataLegend,1,'A2');
xlswrite(ExcelFilename,dataLegend,2,'A2');
xlswrite(ExcelFilename,tlambda,1,'A3');
xlswrite(ExcelFilename,haadfIntensity,2,'A3');
```

A.3. The Monte Carlo Temperature Error Estimation Script

Assessment of the error in temperature as measured by the fitted calibration curve was complicated by the need to incorporate the uncertainty in the original measured values of $(\boldsymbol{S}/\boldsymbol{S}_0)/(t/\lambda)$ shown in Figure 4-9. For the sake of speed and relative ease, we implemented a Monte Carlo method of estimating the uncertainty in a MATLAB script. The script worked by creating a Gaussian variable for each of the four experimentally measured points of thickness-normalized HAADF signal $(\boldsymbol{S}/\boldsymbol{S}_0)/(t/\lambda)$ versus temperature T. The variables had the same mean and standard deviation as the experimental points shown in Figure 4-9. The script then repeats the following process 3000 times:

1. The four variables were each sampled once.
2. An exponential fit of the same form as the calibration curve described in Equation (4-1) was performed to give coefficients for a calibration curve.
3. The obtained curve is used to generate a temperature value for each of a selected set of 28 different values of $(\boldsymbol{S}/\boldsymbol{S}_0)/(t/\lambda)$ distributed across the experimental temperature range.

This process yielded a set of 3000 temperature values for each of the 28 values of $(\boldsymbol{S}/\boldsymbol{S}_0)/(t/\lambda)$, and 3000 sets of coefficients from the fits. The script then exported all the

values to Microsoft Excel: the coefficients, the 28 values of $(\boldsymbol{S}/\boldsymbol{S}_0)/(t/\lambda)$, and the 3000 temperature values for each value of $(\boldsymbol{S}/\boldsymbol{S}_0)/(t/\lambda)$. At this point the script execution ended.

In Excel, after the script finished, a mean and sample standard deviation was calculated for the 3000 temperatures associated with each value of $(\boldsymbol{S}/\boldsymbol{S}_0)/(t/\lambda)$. An upper and lower error were then calculated for each $(\boldsymbol{S}/\boldsymbol{S}_0)/(t/\lambda)$ by adding and subtracting the standard deviation from the mean T. This set of errors versus $(\boldsymbol{S}/\boldsymbol{S}_0)/(t/\lambda)$ was then incorporated into the plot of Figure 4-9.

The quality of the curve fit produced by the script was validated through comparison to the fit produced by the software application Logger Pro 3.16.2. This was accomplished by ensuring that, when given the experimentally measured data points shown in Figure 4-9, the script produced coefficients matching those from Logger Pro to better than three significant figures.

A.4. The Monte Carlo Temperature Error Estimation Script Code

```
%Script for measuring uncertainty of temperature using a Monte Carlo approach

t0=clock;
%Set options for the least-squares nonlinear solver 'lsqnonlin'
options=optimoptions('lsqnonlin','Algorithm','levenberg-
marquardt','Display','off','FunctionTolerance',1.0e-08,...

'MaxFunctionEvaluations',100000,'MaxIterations',10000,'OptimalityTolerance',1
.0e-08,'StepTolerance',1.0e-08);
% The original data points from experiment for (S/S0)/(t/lambda)
%point294 = 0.08705; %std dev 0.0001340
%point225 = 0.08617; %std dev 0.0003221
%point157 = 0.08423; %std dev 0.0001734
%point89 = 0.07966; %std dev 0.0001521

numSamples = 3000; % the number of fits to compute

%values of doubly-normalized HAADF signal at which to measure the uncertainty
in Temperature
haadfSamples=[0.07925, 0.07966, 0.08000, 0.08100, 0.08150, 0.08200, 0.08250,
0.08300, 0.08350, 0.08400,...
    0.08423, 0.08470, 0.08500, 0.08530 0.08555, 0.08575, 0.08600, 0.08617,
0.08635, 0.08650, 0.08670,...
```

```
    0.08690, 0.08705, 0.08710, 0.08720, 0.08730, 0.08740, 0.08750];
temperatureSamples=zeros(numSamples,size(haadfSamples,2));

fitCoeff = zeros(numSamples,3); %initialize fit coefficients

% the loop: sample inputs->fit curve->measure T->repeat
for runCount = 1:1:numSamples
% the original data points as
point294 = normrnd(0.08705,0.0001340);
point225 = normrnd(0.08617,0.0003221);
point157 = normrnd(0.08423,0.0001734);
point89 = normrnd(0.07966,0.0001521);

upperBounds = [+Inf,+Inf,+Inf];
lowerBounds = [-Inf,-Inf,-Inf];
dnHAADF = [point89, point157, point225, point294];
expTemperature = [89.0, 157.0, 225.0, 294.0];

guessCoeff = [-0.0241,-0.0124,0.0877]; %starting guesses for fit coefficients
from original model fit

%generalExp=fittype('a*exp(b*temperature)+c','dependent',{'dnhaadf'},'indepen
dent',{'temperature'},'coefficients',{'a','b','c'});
%testfit=fit(temperature,dnhaadf,generalExp);

expFunct = @(coeff,independentVar)
coeff(1).*exp(coeff(2).*independentVar)+coeff(3); %defines function to fit,
Aexp(BT)+C in terms of temperature and coefficient array
nrmrsd = @(coeff) norm(dnHAADF-expFunct(coeff,expTemperature)); %defines
normalized residual cost function
%[fitCoeff,normalizedResiduals] = fminsearch(nrmrsd,guessCoeff); %fminsearch
doesn't give as good a fit as Logger Pro, had to switch to lsqnonlin
[fitCoeff(runCount,:),normalizedResiduals] =
lsqnonlin(nrmrsd,guessCoeff,lowerBounds,upperBounds,options);
%disp(fitCoeff(runCount,:));
aa=fitCoeff(runCount,1);
bb=fitCoeff(runCount,2);
cc=fitCoeff(runCount,3);
for i = 1:1:size(haadfSamples,2)
    temperatureSamples(runCount,i)=(1/bb)*log((haadfSamples(i)/aa)-(cc/aa));
end %for i
%disp(temperatureSamples(runCount,:));
%plot the monte carlo data points and the fit
%x_plot_range = linspace(min(expTemperature),max(expTemperature));
%figure(1)
%plot(expTemperature,dnHAADF,'pg')
%hold on
%plot(x_plot_range,expFunct(fitCoeff,x_plot_range), '-r')
%hold off
%grid
%xlabel('Temperature')
%ylabel('Doubly Normalized HAADF Signal')
%legend('Inputs','Fit')
end %for runCount
```

```
outFilename="";
outFilename = "Temperature_uncertainty_results"
save(strcat(outFilename,".mat"),'haadfSamples','fitCoeff','temperatureSamples
')
ExcelFilename = strcat(outFilename,".xls")
xlswrite(ExcelFilename,fitCoeff,1,'A4');
xlswrite(ExcelFilename,haadfSamples,2,'B6');
xlswrite(ExcelFilename,temperatureSamples,2,'B7');
disp ('Elapsed clock time (minutes) to run routine is ')
    (etime(clock,t0))/60
```

Appendix B The Many Faces of the Debye-Waller Factor

In compiling the information for this research, we discovered a number of differing expressions for the Debye-Waller (DW) factor W. The Debye-Waller factor appears frequently in thermally-driven wave scattering models, usually as an exponent, for example, e^{-W} or e^{-2W}. These permutations appearing in different sources led to confusion, and required additional research to understand and resolve the different notations and formulations. To compound the confusion, in some sources the factor is represented as M rather than W.

Before enumerating the various forms we found the DW factor could take, some explanation of the terms involved may help. In standard diffraction construction, $\overrightarrow{K_0}$ is the incident beam vector and $\vec{K}$ is the diffracted beam vector in reciprocal space, both starting from the origin. The difference between the two is the diffraction vector $\vec{g} = \vec{K} - \overrightarrow{K_0}$. The scattering vector $\vec{s}$ is defined as $\vec{s} = \vec{g}/2$. The magnitudes of those two vectors shares the

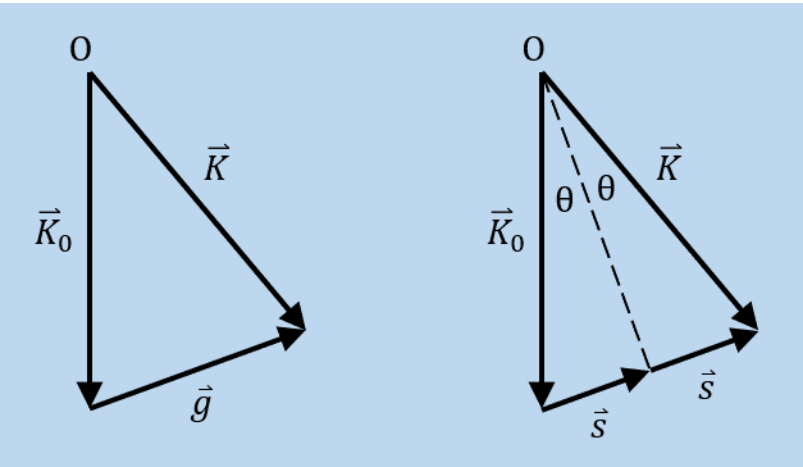

Figure B-1: Illustration of the relationships between various vectors in standard diffraction notation (after Williams & Carter [24]).

same relationship: $s = g/2$. The scattering angle θ, in turn, is the angle subtended by $\vec{s}$ from the origin, and when Bragg diffraction conditions are satisfied it equals the Bragg angle θ_B.

As given in Section 2.2, the magnitude of the diffraction vector $\vec{s}$ is $s = \sin(\theta)/\lambda_B$, where λ_B is the wavelength of the scattered radiation.

$$W = 2\pi^2\langle u_s\rangle^2 g^2$$

$$W = 8\pi^2\langle u_s\rangle^2 s^2$$

$$W = 8\pi^2\langle u_s\rangle^2(\sin(\theta)/\lambda_B)^2$$

Finally, if we introduce the Temperature Parameter B, which is defined as $B = 8\pi^2\langle u_s\rangle^2$, we get the following:

$$W = Bs^2$$

$$W = B(\sin(\theta)/\lambda_B)^2$$

Hopefully this primer will be an aid to anyone who follows on in this line of research.